Near field evolution of wingtip vortices under synthetic-jet based control

Original
Near field evolution of wingtip vortices under synthetic-jet based control / Zaccara, M., Paolillo, G., Cafiero, G., Astarita, T., Iuso, G., Cardone, G., Greco, C.S.. - In: AEROSPACE SCIENCE AND TECHNOLOGY. - ISSN 1270-9638. - 148:(2024). [10.1016/j.ast.2024.109068]

Publisher:
Elsevier

Published
DOI:10.1016/j.ast.2024.109068

Aerospace Science and Technology 148 (2024) 109068

Contents lists available at ScienceDirect

Aerospace Science and Technology

journal homepage: www.elsevier.com/locate/aescte

Near field evolution of wingtip vortices under synthetic-jet based control

Mirko Zaccara [a], Gerardo Paolillo [a], Gioacchino Cafiero [b], Tommaso Astarita [a], Gaetano Iuso [b], Gennaro Cardone [a], Carlo Salvatore Greco [a,*]

[a] *Università degli Studi di Napoli "Federico II", Dipartimento di Ingegneria Industriale, Piazzale Tecchio 80, 80125, Napoli, Italy*
[b] *Dipartimento di Ingegneria Meccanica ed Aerospaziale, Politecnico di Torino, Corso Duca degli Abruzzi 24, 10129, Torino, Italy*

ARTICLE INFO

Communicated by Damiano Casalino

Keywords:
Synthetic jet
Wingtip vortices
Flow control
PIV

ABSTRACT

The present research focuses on the experimental investigation of the effectiveness of synthetic jet actuation on a pair of counter-rotating vortices generated by an unswept, low aspect ratio, squared-tipped wing in order to preserve the mutual induction during their evolution. The synthetic jet is actuated at Crow and Widnall's instability frequencies ($F^+ = 0.071,\ 0.55$) and at a fixed momentum coefficient $C_\mu = 0.2\%$ with the goal of reducing the vortex strength and the induced circumferential velocity. The effect of the jet exit section area, and thus the characteristic jet velocity, has been investigated by testing three wing models equipped with a synthetic jet issuing through a rectangular slot of constant length and three different values of the height, equal to 0.01, 0.02, and 0.04 chord lengths, respectively. A phase-locked stereoscopic particle image velocimetry setup has been designed and implemented to carry out a parametric study in the near wake of the wing models at four downstream distances from the wing trailing edge, namely equal to 0.1, 0.5, 1 and 2 chord lengths.

The slot with a height to chord ratio of 4%, yields the minimum vorticity level, the maximum vortex diffusion with a diameter up to 3 times greater than the baseline reference value, and lower values of the vortex circulation. This effect, together with the periodic motion along a ±45° direction experienced by the vortex after the synthetic jet blowing, is beneficial in terms of an anticipated instability of the tip vortices as well as of the mitigation of the blade-vortex-interaction in propellers.

1. Introduction

Wingtip vortices are a byproduct of lift generation on finite-span lifting wings and they come with many adverse effects spanning various applications. In fact, the aviation industry has been concerned for decades with their drawbacks such as wake hazard, induced drag, and Blade-Vortex Interaction (BVI) noise. With regard to the first one, if a smaller aircraft encounters the strong vortices shed from a larger plane, the angular momentum from the vortices may induce a large destabilizing moment, which can cause an irrecoverable loss of control [1]. To overcome this, aviation regulations mandate strict distances that are dependent on the size of the leading and trailing aircraft. Owing to the presence of the wingtip vortices, the freestream kinetic energy is transferred into rotational one producing a downwash in the wake of the wing. As a consequence, the induced drag is produced which accounts for up to 40% of the aircraft's total drag [2]. Helicopter main rotor blades represent another area where vortex-structure interaction could compromise the structural integrity of the blades. During the rotation, each rotor blade sheds a tip vortex which can interact with the following blades and the tail-rotor blades. This interaction, known as Blade-Vortex Interaction (BVI), results in large unsteady forces due to rapid changes in local velocity around the blades, leading to an enhanced rotor-blade fatigue and noise source [3,4]. In general, three ways are conceivable to reduce the BVI noise: increasing the distance between the tip vortex and the blade; reducing the blade load when the vortex interaction occurs; decreasing the tip vortex strength. In this framework, researchers proposed innovative blade tip designs [5] trying to deflect the vortex avoiding the impact with the following blade and the use of wingtip devices to weaken the tip vortex such as sub-wing [6–8], end-plate tip [7], vane tip [9], tip spoiler [10], canard tip [11], and wingtip blowing [12–15].

Significant efforts have been devoted over the years trying to control the adverse effects of trailing vortices [16,2]. The most common alleviation schemes rely on altering the thickness, turbulence, and longitudinal velocities in the vortex core. It has been proven by Bailey and Tavoularis [17] that injecting turbulence into the free-stream increases

---

* Corresponding author.
E-mail address: carlosalvatore.greco@unina.it (C.S. Greco).

https://doi.org/10.1016/j.ast.2024.109068
Received 13 June 2023; Received in revised form 7 November 2023; Accepted 10 March 2024

Nomenclature

Acronyms

3C	Three Components
2D	Two Dimensional
3D	Three Dimensional
BCs	Squared wing Baseline Case
BVI	Blade Vortex Interaction
PIV	Particle Image Velocimetry
sCMOS	scientific Complementary Metal-Oxide-Semiconductor
SJ	Synthetic Jet
S-PIV	Stereoscopic Particle Image Velocimetry
Ss01	Squared wing with synthetic jet slot height of 1% of the chord length
Ss02	Squared wing with synthetic jet slot height of 2% of the chord length
Ss04	Squared wing with synthetic jet slot height of 4% of the chord length
ZNMF	Zero-Net-Mass-Flux

Roman letters

A_j	synthetic jet exit section area	m^2
$A_{w/2}$	half-wing surface area	m^2
b	wing span	m
c	wing chord	m
D_e	equivalent hydraulic diameter	m
D_{max}, D_{min}	Major and minor axes of the vortex	m
d	downstream distance of the measurement plane	m
d_p	tracer particle diameter	m
$\hat{e}_z$	unit vector normal to the measurement plane	
f	frequency	Hz
f_a	actuation frequency	Hz
$f_\#$	camera f-number	
L_e	equivalent length	m
L_m	measurement resolution	m
$Oxyz$	Physical reference frame	
$O'x'y'$	Vortex centered reference frame	
PM	spatial vector from the center point P to a point M	
p_j	synthetic jet exit section perimeter	m
r	radial coordinate	m
r_c	vortex core radius	m
S	surface area for computation of Γ_1	m^2
T	synthetic jet actuation period	s
U_0	characteristic velocity of the synthetic jet	m/s
U_θ	circumferential velocity	m/s
U_∞	free-stream flow velocity	m/s
u_c	spanwise velocity of the vortex center	m/s
u_M	total velocity vector at point M	m/s
u_e	velocity along the jet centerline at the exit section	m/s
u, v, w	velocity component in the Cartersian reference frame	m/s
v_c	transverse velocity of the vortex center	m/s
x_0, y_0	Vortex center coordinates	m

Greek letters

α	geometrical angle of attack	°
Γ	vortex circulation	m^2/s
Γ^{BCs}	vortex circulation of the baseline case	m^2/s
Γ_c	vortex core circulation	m^2/s
Γ_1	scalar function for vortex identification	
ζ_z	streamwise vorticity	1/s
$\zeta_{z,max}$	maximum streamwise vorticity	1/s
$\zeta_{z,max}^{BCs}$	maximum streamwise vorticity of the baseline case	1/s
λ	wavelength	m
μ_∞	free-stream dynamic viscosity	Pa·s
θ	azimuthal coordinate	rad
ρ_∞	free-stream flow density	$\mathrm{kg/m}^3$
ρ_j	jet density	$\mathrm{kg/m}^3$
τ_s	tracer particle relaxation time	s
Φ	vortex inclination angle	°
ϕ	phase of the synthetic jet signal	°
ϕ_e	phase of the electrical signal	°

Dimensionless parameters

C_μ	momentum coefficient, $\left(A_j \rho_j U_0^2\right) / \left(A_{w/2} \rho_\infty U_\infty^2\right)$
η	self-similar variable, r/r_c
F^+	dimensionless frequency, $f_a c / U_\infty$
Re_c	chord Reynolds number, $\left(\rho_\infty U_\infty c\right) / \mu_\infty$
St	Stokes number, $\left(\tau_s U_\infty\right) / d_p$

the vortex wandering and the rate of decay of the peak tangential velocity. Since creating upstream turbulence in the flight-path of an airplane is not a practical method, different methods have been extensively studied to inject turbulence into a wingtip vortex such as: use of structural modification of the wingtip (i.e. winglets) and/or along the trailing edge of the wings and flaps; blowing or suction in the vicinity of the wingtip; excitation of the inherent instabilities of the tip vortices, commonly referred to as Crow [18] and Widnall [19–21] instabilities. The control techniques implementing the aforementioned methods are generally distinguished between passive and active.

Most of the early research into passively solving the wake vortex hazard involved a modification of the wake structure before roll-up by changing the geometry of the wing, thus changing the load distribution. Rossow [22] performed theoretical studies using 2D inviscid computations to determine the optimized loading distribution which would result in a wake that would either not roll-up or be more diffused. Linear load distribution from root to tip as well as with abrupt variation in lift resulted in a diffused vorticity field with a noticeable decrease in the induced rolling moment that would be encountered by the following aircraft. Also a notched load distribution has been demonstrated to result in a more diffused wake by Graham et al. [23]. Corsiglia and Dunham [24] performed experiments both on ground-based facilities and flight tests on a full scale Boeing 747 showing that a less hazardous wake can be obtained by shifting the wing center of pressure inward. In addition to geometric modification of the wings, a variety of experiments were performed on adding static devices to already existing planforms: splines mounted directly downstream of the wing tip [25] and different wing tip shapes [26]; spoilers installed on the suction side of wings [27]; fins (i.e., winglets) mounted on the suction or pressure side of wings [28–31]. The use of such devices is still aimed at modifying the load distribution and/or adding another discrete vortex to the wake that might interact with the tip vortex in a beneficial way.

Active wake alleviation strategies rely upon some time-dependent forcing to perturb the aircraft wake and excite its inherent instabilities to promote a faster decay. Furthermore, active flow control in principle allows to optimize the wake alleviation throughout the entire flight envelope. The first attempts to implement active flow control of the wingtip vortices were based on time-dependent lift distributions triggered by oscillations of the elevator [32,33], periodic flap oscillations [34], lateral-control and roll oscillations [35–37], oscillating ailerons [38], and segmented Gurney flaps [39]. Although an anticipated wake dissipation has been demonstrated to be achievable, the excessive level of oscillations makes the former strategies not feasible during take-off or landing [35] especially because of the associated passenger discomfort [37]. Furthermore, the oscillation of the lift distribution could lead to a coupling with the wing bending mode, with associated structural issues that need to be taken into account during the design process.

More recent active flow control techniques rely on exhausting mass and momentum in the vicinity of the wingtip to control the formation of the trailing vortex. In this case, the drawback is to harvest the mass injected, usually bleeding it from the engine, which reduces its efficiency during take-off and cruise, although not during landing when the engines are generally idling. To overcome this shortcoming, Zero-Net-Mass-Flux (ZNMF) devices (e.g. synthetic jets, plasma actuators, etc.) for momentum injection might represent an interesting solution. On the other hand, these devices lack the control authority of net mass flux devices and therefore they carry their own set of challenges [40].

In the last years, Edstrand and Cattafesta [41] performed PIV experiments on the effects of uniform and segmented steady blowing from the wing suction side. Garcìa-Ortiz et al. [42] investigated the effects of continuous blowing through a small orifice up to 20 chord-lengths downstream. Although the wingtip vortex strength is highly decreased at a Reynolds number based on the chord $Re_c = 7 \cdot 10^3$, scaling at larger values of Re_c showed poor performance. Using steady and pulsed jets from discrete ports on the wingtip, Heyes and Smith [43] studied the effect of blowing on the vortex position. They showed striking effects on the vortex structure resulting in a higher core size and a reduced induced velocity peak. This was the first work with the goal of introducing vortex perturbations tuned to the inherent flow instability frequencies, accelerating the vortex break up.

As already mentioned, the use of zero-net-mass-flux devices, such as synthetic jets (SJs), allows the injection of turbulence, momentum, and vorticity into the flow with a variable frequency tuned to match the inherent flow instabilities on the wingtip vortices avoiding any bleed from the engine. In order to analyze the effectiveness of SJs actuation and for comparison purposes in the wingtip vortices literature, two dimensionless control parameters are taken into account, the SJ momentum coefficient and the dimensionless actuation frequency, which are respectively defined as

$$C_\mu = \frac{A_j}{A_{w/2}} \frac{\rho_j U_0^2}{\rho_\infty U_\infty^2}, \qquad F^+ = \frac{f_a c}{U_\infty} \tag{1}$$

where A_j is the exit section area of the jet, $A_{w/2}$ is the half-wing surface, ρ_j and ρ_∞ are the jet and freestream densities, U_∞ is the freestream velocity, c is the wing chord-length and f_a is the jet actuation frequency. In the present work, following Smith and Glezer [44], the characteristic jet velocity U_0 is defined as the mean centerline velocity over the portion of the cycle corresponding to the ejection

$$U_0 = \frac{1}{T} \int_0^{\frac{T}{2}} u_e(t)\, dt \tag{2}$$

where T is the SJ actuation period and u_e is the velocity along the jet centerline at the exit section.

In the literature, there are few examples of application of SJs to the control of the wing tip vortices. Margaris and Gursul [45,46] conducted a parametric PIV investigation on the effect of both continuous and synthetic jets blowing from slots located at the leading and/or trailing edge of a NACA 0015 with both a squared and rounded wingtips. They observed that the jet produced one or more counter-rotating vortices that typically merged with the primary vortex, reducing its strength up to 50% ($C_\mu = 0.016\%$, $F^+ = 0.75$). Dghim et al. [47–49] reported a detailed investigation of the effectiveness of SJ actuation in the near and mid-wake development of a wingtip vortex. They demonstrated that blowing at actuation frequencies in the range corresponding to Crow and Widnall's instability frequencies leads to the best results in terms of decreased pressure coefficient distribution at the wingtip, while a vorticity peak reduction up to 60% is obtained by increasing the values of the control momentum coefficient up to $C_\mu = 1\%$. They also investigated the effects of the blowing slot shape by comparing the performance of a spanwise straight and a curved nozzle. They observed in both cases a reduction of the tangential velocity peak and an increase of the vortex core size, with the straight SJ nozzle outperforming the curved one due to the larger turbulence level introduced into the flow. More recently, Zaccara et al. [50] conducted a parametric study on the effectiveness of the SJ control on wingtip vortices by varying C_μ and F^+. Promising results were obtained by observing a maximum reduction of 46% on the peak value for the configuration with $C_\mu = 0.04\%$ and $F^+ = 0.735$ in time-averaged evolution. Phase-averaged measurements were carried out and revealed a clear relation between the SJ blowing and suction phases and the periodic variation of the vortices features.

The present work fits into the wake of the previous investigation and aims at investigating the effects of the SJ slot geometry on the control of the wingtip vortices generated by a finite-span wing. The active control is carried out by triggering the inherent Crow and Widnall instabilities varying the SJ operating frequency at fixed momentum coefficient $C_\mu = 0.2\%$. The effects of the jet exit section area, and thus the characteristic jet velocity, are investigated by testing three wing models equipped with a synthetic jet rectangular slot of constant length, lying in the chord plane, with an increasing height of 0.01, 0.02, and 0.04 chord lengths respectively. Stereoscopic particle image velocimetry (S-PIV) measurements are carried out in different crosswise planes located in the near wake at a downstream distance from the wing trailing edge of 0.1, 0.5, 1 and 2 chord lengths. As in the authors' previous work [50], a phase-locked analysis is conducted to give clear insight of the development of the wingtip vortices under the SJ actuation.

It is remarked that the goal of the present investigation is to evaluate the sensitivity of the wing-tip vortex structure to the SJ actuation when varying the slot geometry. The assessment of the influence from the SJ control on the streamwise development of the actuated vortex and the enhancement of its inherent instabilities is addressed in a follow-up article [51] in which S-PIV measurements in the far wake of the wing model are presented and comprehensively analyzed.

2. Experimental rig

2.1. Wind tunnel and wing model

The measurements were conducted in the closed-circuit subsonic wind tunnel "D3M" located in the "Modesto Panetti" laboratory of the Mechanical and Aerospace Engineering Department at Politecnico di Torino (Italy). The test chamber has a circular section with a diameter of 3 m and a length of 5 m, with a small divergence to compensate the growth of the boundary layer on the wind tunnel walls. The flow then circulates throughout the tunnel, with diverging sections and straightening vanes in the corners to guide their rotations, until reaching the convergent before the test chamber with a contraction ratio of 2.33. The maximum speed achievable in this facility is 90 m/s, while the turbulence intensity is 0.4% [52]. For the present investigation, the free-stream velocity has been set to $U_\infty = 12$ m/s, corresponding to a Reynolds number based on the wing chord of $Re_c = 1.20 \times 10^5$.

The assembly employed for the near-wake measurements is shown in Fig. 1. Starting from the bottom, the wing assembly is anchored to the wind tunnel through a squared steel base. In order to properly align the wing to the mean flow direction, an angle regulation system based on three pillars has been designed to allow pitch and yaw regulations of ±10° and ±5°, respectively, and setting of a zero roll angle.

The loudspeaker for the SJ generation and its cavity are mounted directly on the base of the wing sting, made of carbon fiber, which is attached to the pillars through a steel interface plate. The wing sting has a constant airfoil section NACA 0024, with a chord of 0.149 m, and a span of 1.064 m and it is made of carbon fiber with a wall thickness of 0.004 m in order to create a sufficiently large duct. Finally, an interchangeable wing is mounted on the top by interference and the different

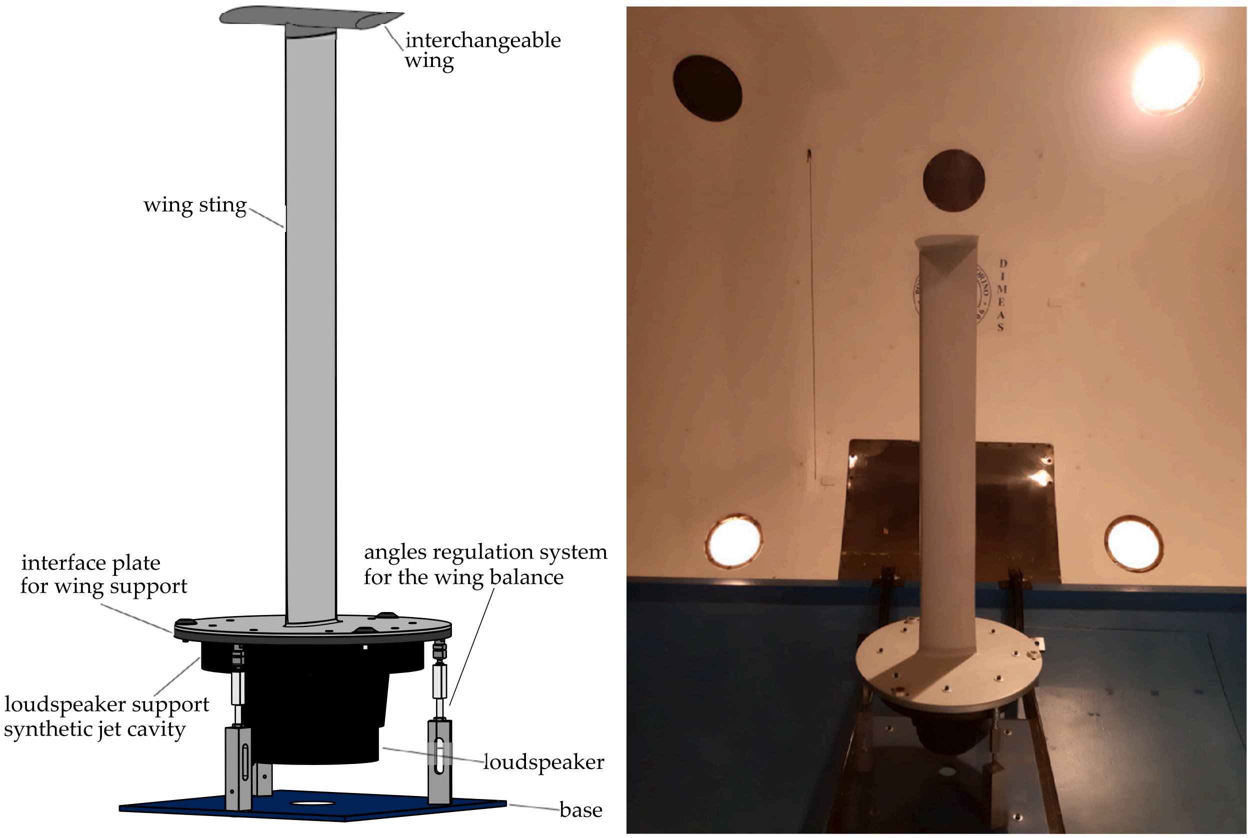

Fig. 1. Wing assembly setup in the D3M wind tunnel.

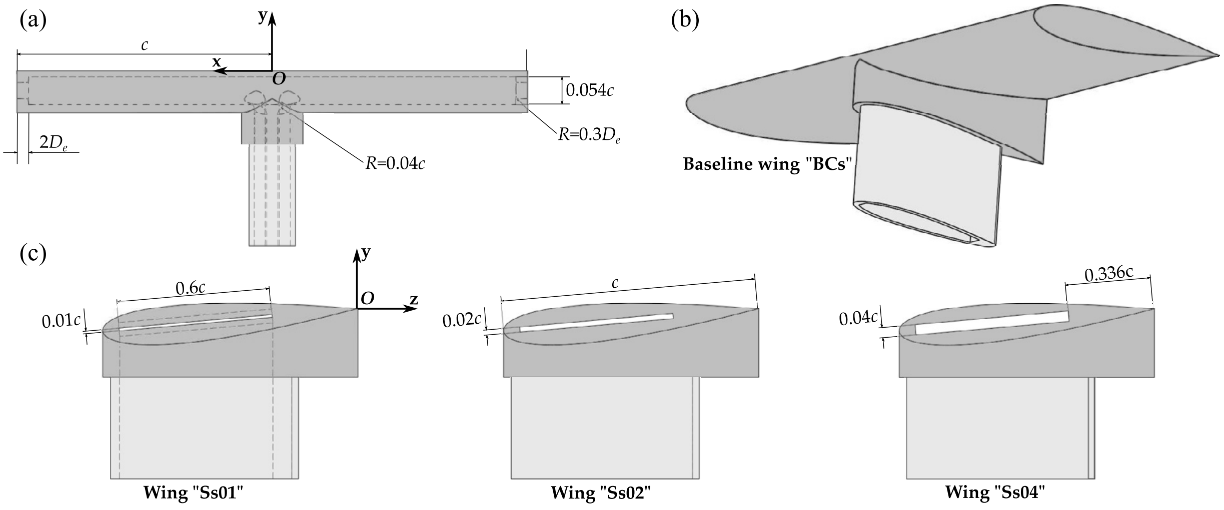

Fig. 2. Sketch of the interchangeable wings with different synthetic jet exit sections: (a) front view, (b) 3d view, (c) lateral view with detail of the exit slot. The dashed lines are representative of the internal geometry of the SJ duct.

wing models employed are shown in Fig. 2. Each model is a rectangular finite-span square-tipped wing with a NACA 0015 airfoil section. The airfoil chord is $c = 0.15$ m, the wingspan is $b = 2c = 0.30$ m, resulting in an aspect ratio of 2. The model solid blockage, accounting for both the wing model and the wing sting, is equal to 0.64%, thus its effects on the present results can be neglected. The wings were manufactured in polyamide PA 2200 by a selective laser sintering 3D EOS printer. Then, they were painted and their surface finish polished; no tripping is applied to the lower and upper wing surface. The angle of attack is set to $\alpha = -5°$. As a result, the wing assembly was mounted in the wind tunnel by aligning the wing sting to be at 0° of yaw, pitch, and roll with respect to the streamwise direction with the aid of an inertial measurement unit. The choice of a negative angle of attack minimizes the possible influence of the wing sting wake on the wingtip vortices which develops inboard and upward going downstream.

Four different wing models were tested in the present investigation: the reference wing and three models with a rectangular SJ exit section with the same width of $0.6c$ and heights of $0.01c$, $0.02c$, and $0.04c$ respectively. In each configuration, the slot lies in the chord plane. Hereinafter, they will be referred to as “BCs” (Squared wing Baseline Case), “Ss01” (Squared wing with SJ slot height of 1% of the chord length), “Ss02” (Squared wing with SJ slot height of 2% of the chord

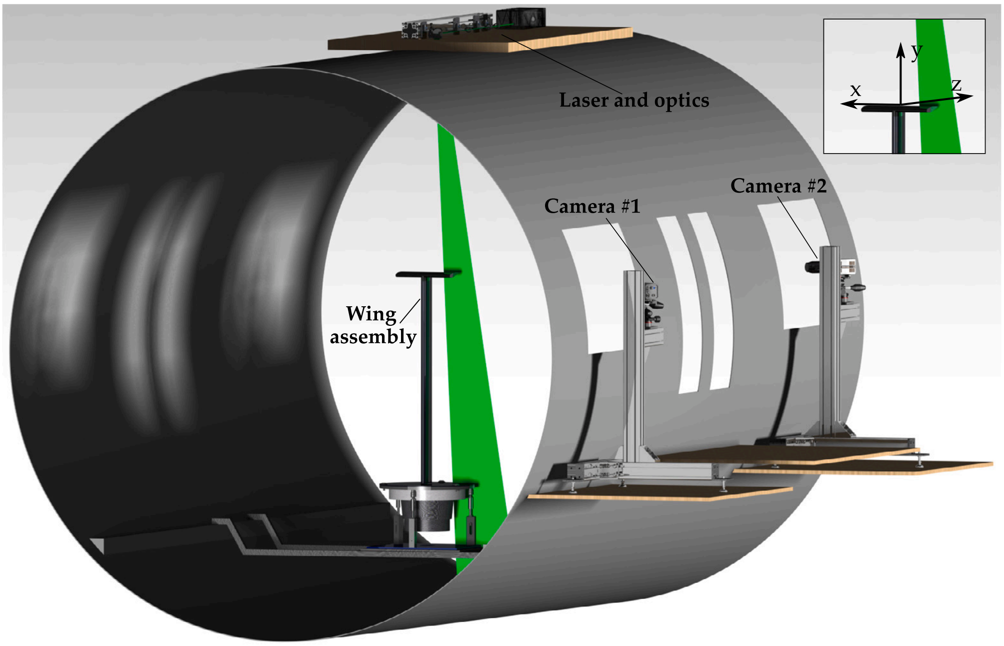

Fig. 3. Experimental setup in the D3M wind tunnel.

length) and "Ss04" (Squared wing with SJ slot height of 4% of the chord length).

2.2. Synthetic jet device

The SJ runs throughout the wing sting, turning into a rectangular duct in the wing with a height of $0.054c$ (0.0081 m). It is important to note that both the width and the height of the SJ duct have been chosen in order to maximize the flow area with respect to the minimum wall thickness of the 3D printer employed and by minimizing the head loss due to the flow area variation between the wing sting and the wing. Finally, the rectangular SJ chamber inside the wing ends at the tips with two rectangular ducts with the different heights described before and length equal to $L_e = 2D_e = 2 \cdot 4A_j/p_j$, being D_e the equivalent hydraulic diameter and p_j the perimeter of the SJ exit section. Furthermore, head losses and flow separation effects have been reduced with the aid of appropriate fillets shown in Fig. 2.

The synthetic jet is generated using a 900 W, 12 in subwoofer (Alpine X-W12D4) as oscillating driver [53]. It is supplied with a sinusoidal input signal generated by a Digilent Analog Discovery™ USB Oscilloscope, coupled with a power amplifier (Behringer NX6000D). The subwoofer has been mounted at the base of the wing sting with an insulation sheath to avoid the transmission of the vibrations to the wing and they are dampened also by the large mass of the wing assembly. As a result, the possible effect of vibration has been considered negligible especially in the low power range employed in the experimental tests.

As described in the introduction section, the SJ actuation frequencies have been tuned to the inherent vortices instabilities. By recalling the wavelengths of the Crow [54] and Widnall [19,55,47] instabilities, the following actuation frequencies have been employed:

$$f_{\text{Crow}} = \frac{U_\infty}{\lambda_{\text{Crow}}} \simeq 6\ \text{Hz} \implies F^+ = 0.071 \tag{3a}$$

$$f_{\text{Widnall}} = \frac{U_\infty}{\lambda_{\text{Widnall}}} \simeq 44\ \text{Hz} \implies F^+ = 0.55\,. \tag{3b}$$

At these working frequencies, the impedance of the three SJ configurations differs of less than 4%.

In order to investigate the effect of the SJ exit velocity U_0 on the wingtip vortices control, a constant momentum coefficient $C_\mu = 0.2\%$ (Eq. (1)) has been considered for both frequencies. Since the tested models reported in Fig. 2 present a SJ exit section area increasing by four times from $0.006c^2$ (Ss01) to $0.024c^2$ (Ss04), keeping C_μ constant results in a halved SJ velocity U_0.

A preliminary characterization of the jet issuing through the slots was performed in wind-off conditions. The instantaneous velocity of the synthetic jet at both the tips was measured by means of a constant temperature anemometer system (Dantec-MiniCTA) equipped with a single-component hot wire of length 1.25 mm and diameter 5 µm. It is worth noting that the hot-wire sensor acquisitions, at a sampling frequency fixed to $1000f_a$, were synchronized with the electrical signal sent to the loudspeaker. As a result, the phase shift between this electrical signal and the synthetic jet exit velocity was characterized in order to accurately identify the start of the cycle of the synthetic jet with respect to the sampled phases. Hot-wire measurements were performed at the exit of the synthetic jet in three different locations (1/4, 1/2 and 3/4) along the slot length and at half the height of the slot for both the wing tips. For each location, the time-averaged ejection velocity was calculated and U_0 was assumed equal to the average of all these values. The amplitude of the input voltage signal was varied iteratively until the measured U_0 differed less than 1% from the target value corresponding to the desired C_μ. The relative standard deviation (standard deviation normalized by the average) of the six different measurements was found to be lower than 0.5%.

Lastly, the velocimetry measurements were carried out for each SJ configuration in four different crosswise planes downstream of the wing model. The employed reference frame $Oxyz$ is shown in Fig. 2; the origin is located in the middle of the wing trailing edge, whereas the x, y and z axes are aligned with the spanwise, crosswise (upward) and streamwise directions, respectively. Particle images are acquired in the four planes $z/c = 0.1$, $z/c = 0.5$, $z/c = 1$, and $z/c = 2$, parallel to the xy coordinate plane. In the following, the S-PIV setup and the image processing are described in detail.

2.3. S-PIV setup and image processing

Stereoscopic particle image velocimetry is used to measure the instantaneous two-dimensional three-component (2D-3C) velocity field. A schematic of the experimental setup is shown in Fig. 3. The flow is seeded using the Safex Fog Fluid "Extra Clean" for PIV applications; it is nebulized by a smoke machine Martin Magnum 1200 which produces particles having a mean diameter of 1 μm, thus resulting in a Stokes number $St \ll 1$. The wind tunnel fan guarantees the mixing of the particles in the flow. Illumination is provided by a Quantel Evergreen low-speed double pulsed Nd:YAG laser (532 nm, 200 mJ per pulse, <10 ns pulse duration). The laser beam is shaped into a 2.2 mm thick light sheet. The time delay between the two laser pulses has been set to 20 μs. Particle images are acquired by two Andor Zyla sCMOS cameras (2160×2560 pixels, pixel pitch of 6.5 μm, intensity resolution 16 bit) in stereo configuration equipped with a Nikon Micro-Nikkor lens with a focal length of 200 mm. Both cameras are in side-scattering, with a relative aperture set to $f_\# = 16$. The angle between the optical axes of the two cameras is set to about 86° and 3D-printed Scheimpflug adapters are used in order to achieve uniform focus across the entire field of view. The present imaging produces a field of view of $0.84c \times 0.90c$ with a spatial resolution of 15.8 pixel/mm. The optical camera calibration has been performed by using a target plate made of a regular Cartesian grid of white dots on a black background with a 10 mm spacing on both the front and back surfaces. The mapping functions between the image planes and the measurement plane are determined using a pinhole camera model. The root mean square calibration error is lower than 1.4 pixels for both cameras.

In order to perform phase-locked measurements, the acquisition system is synchronized with the synthetic jet for each investigated controlled case by an external signal synchronizer. In particular, the S-PIV measurements are locked to the electrical signal driving the loudspeaker with a proper sampling frequency estimated according the procedure of Greco et al. [53]. For the present work, the phenomenon is sampled with a phase separation $\Delta\phi = 24°$, leading to 15 phases per cycle. A total of 3750 image pairs, i.e. 250 snapshots per phase, are acquired to obtain statistically reliable data. The quality of the image pairs is improved by subtracting a background intensity from the raw images obtained by computing the historical minimum intensity based on the entire ensemble of the image pairs.

A multiple-pass algorithm with image deformation is employed to compute the velocity field using Blackman weighting windows according to Astarita and Cardone [56], and Astarita [57–59]. The final interrogation area size is 96×96 pixels corresponding to an equivalent 48×48 top-hat interrogation window [58], with an overlap of 66.7%, resulting in a measurement resolution L_m of about 2 mm. This is enough to resolve accurately the inner core of the wing-tip vortex [60,61]. The minimum core radius of the wing tip vortex detected in the phase-averaged velocity field is equal to 6.0 mm, whereas the average core radius is 9.6 mm. Therefore, $L_m/r_c \leq 0.33$ and on the average the ratio L_m/r_c is equal to 0.21. The latter value is only slightly greater than the threshold value ($L_m/r_c < 0.2$) suggested in [62] and [63] for accurate measurements of the core radius. Lastly, the maximum random error on the instantaneous velocity vectors is estimated to be 0.106 pixels [64], which leads to a vorticity uncertainty of about 2.3% of the maximum detected phase-averaged vorticity [65].

3. Data processing and metrics

3.1. Vortex identification method

Different vortex identification methods have been proposed over the years such as the swirling strength scheme [66], Q and λ_2 criteria [67], and the geometric center approach [60]. Several reviews of the most common vortex identification techniques have been reported in the literature [68,69]. The method used in the present study is that proposed by Graftieaux et al. [70] and is based on the computation of a non-Galilean invariant approach. In particular, it is based on the evaluation of the scalar function $\Gamma_1(P)$ as follows:

$$\Gamma_1(P) = \frac{1}{N}\sum_S \frac{\left(PM \times u_M\right)\cdot \hat{e}_z}{|PM|\,|u_M|} \tag{4}$$

where PM is the vector from the center point P to a point M in the region S, which may be of any arbitrary shape that includes the point P for a determination of $\Gamma_1(P)$. Furthermore, u_M is the velocity vector at point M while $\hat{e}_z$ is the unit vector normal to the measurement plane. The vortex center corresponds to the measurement point where the value of the scalar function Γ_1 is maximum. In particular, the Γ_1 function was conceived in order to separate the velocity fluctuations caused by large-scale vortices from those related to small-scale turbulence [70–72].

3.2. Vortex model

The geometrical and physical characteristics of a single wingtip vortex are accurately evaluated by fitting the experimental streamwise vorticity field to the following two-dimensional elliptical Gaussian model:

$$\zeta_z(x,y) = \zeta_{z,max}\exp\left[-\left(\frac{x'^2}{D_{max}^2/8} + \frac{y'^2}{D_{min}^2/8}\right)\right] \tag{5}$$

where $\zeta_{z,max}$ is the streamwise vorticity peak, D_{max} and D_{min} are the major and minor axes of the elliptical vortex core region and x', y' are the coordinates along the vortex principal axis directions and are related to the wing-body coordinates via the following transformation:

$$\begin{bmatrix} x' \\ y' \end{bmatrix} = \begin{bmatrix} \cos\Phi & \sin\Phi \\ -\sin\Phi & \cos\Phi \end{bmatrix}\begin{bmatrix} x - x_0 \\ y - y_0 \end{bmatrix}, \tag{6}$$

with x_0 and y_0 being the wing-body coordinates of the vortex center and Φ the angle between the x' (major axis direction) and the x axes.

The geometrical characteristics of the vortex are completely described by the set of parameters D_{max}, D_{min}, and Φ. This approach has been preferred to the Lamb-Oseen vortex model (single Gaussian vorticity profile, [73]) given the capability to pick up non-circular shapes of the vortex.

4. Time-averaged results

In this section, the results of the average based on the entire ensemble of the acquired instantaneous flow fields for each physical quantity will be presented and discussed in terms of the main physical characteristics of the wingtip vortex such as the streamwise vorticity fields, circumferential velocity, and circulation. As regards the notation employed for the velocity components, the small letters u, v, and w indicate the instantaneous velocity components while the operator $\overline{(\cdot)}$ represents time-averaged values.

4.1. Streamwise vorticity and geometrical features

The normalized time-averaged streamwise vorticity fields $\overline{\zeta}_z c/U_\infty$ for the baseline configuration at $z/c = 0.1,\ 0.5,\ 1,\ 2$ are reported in Fig. 4. Two different regions can be identified: the wake shear layer and the tip vortex. The former exhibits a spiral shape with relatively low vorticity levels, whereas the latter contains most of the vorticity within a nearly circular area. Outside the wake and the tip vortex regions, the vorticity is almost zero. At $z/c = 0.1$, the peak value of the normalized streamwise vorticity at the center of the vortex core region is about 10. Half a chordlength downstream, the vorticity has rolled up into a coherent trailing vortex, which is also seen at the last measurement plane with no qualitative changes. However, the vortex moves inboard and upward at downstream locations with a peak value decreasing down to 50% at $z/c = 2$.

In order to obtain a good understanding of the effect of the SJ actuation with an increasing jet velocity, the contours of $\overline{\zeta}_z c/U_\infty$ for the controlled case at $F^+ = 0.071$ and $F^+ = 0.55$ for the model Ss01 and Ss04 respectively are examined in Fig. 5. The horizontal dashed black line represents the projection of the wing trailing edge.

For the controlled case at $C_\mu = 0.2\%$, $F^+ = 0.071$ and the wing model Ss01 (Fig. 5a, 5b, 5c, and 5d), two main vortices, which are the

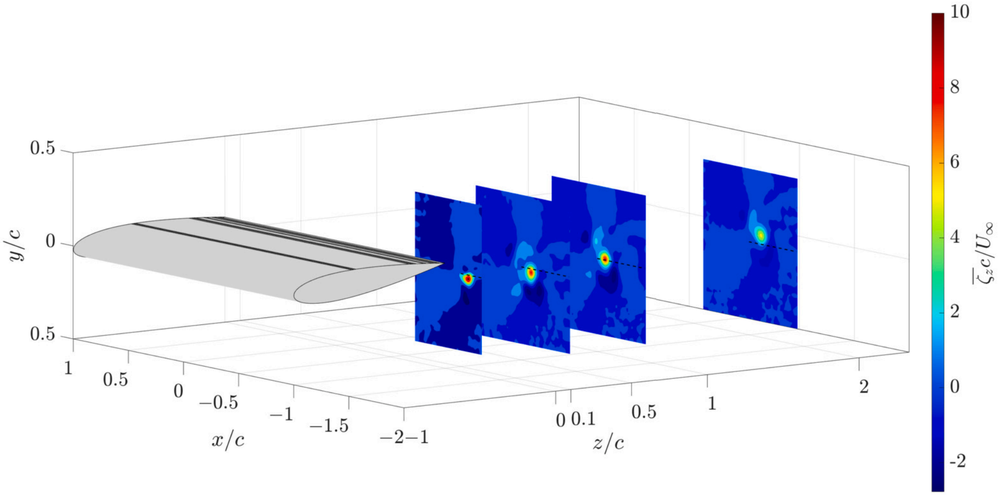

Fig. 4. Time-averaged streamwise vorticity fields for the baseline configuration BCs. Measurement planes at $z/c = 0.1,\ 0.5,\ 1$ and 2. The dashed lines represent the intersections with the reference $y = 0$ plane, i.e. the projections of the trailing edge on the same planes. (For interpretation of the colors in the figure(s), the reader is referred to the web version of this article.)

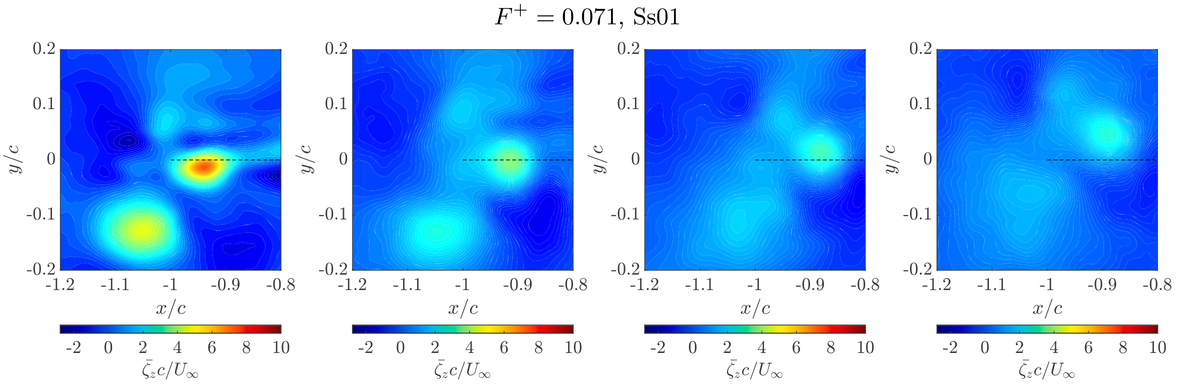

(a) $z/c = 0.1$ (b) $z/c = 0.5$ (c) $z/c = 1$ (d) $z/c = 2$

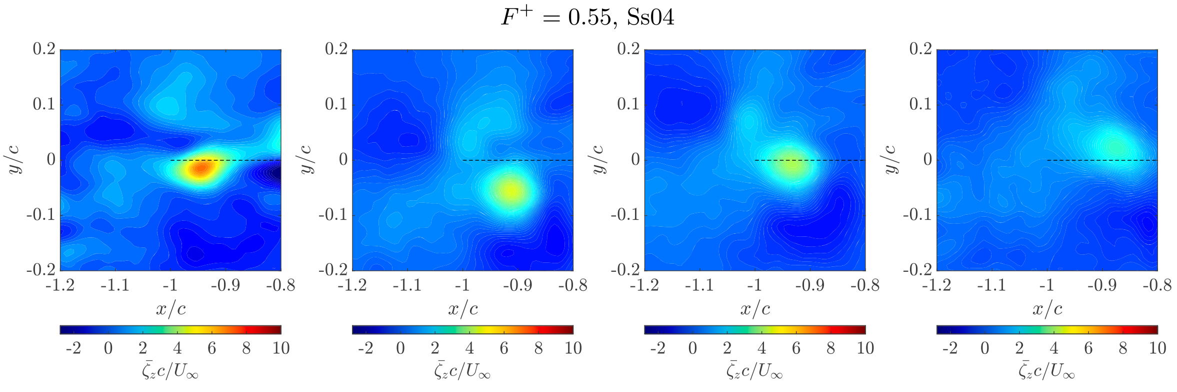

(e) $z/c = 0.1$ (f) $z/c = 0.5$ (g) $z/c = 1$ (h) $z/c = 2$

Fig. 5. Contour maps of the normalized time-averaged streamwise vorticity fields at different streamwise locations for the controlled cases with $C_\mu = 0.2\%$ and: (a-d) $F^+ = 0.071$ for the model Ss01; (e-h) $F^+ = 0.55$ for the model Ss04.

wingtip vortex and the co-rotating jet vortex, are clearly visible. The interaction between these two co-rotating vortices downstream of the trailing edge characterizes the near wake depending on their strengths and initial location. As it can be noted, the strength of the jet vortex is three times lower than the tip one and it almost vanishes at $z/c = 2$. The presence of the co-rotating jet vortex is in agreement with the findings of Margaris and Gursul [46]. The effectiveness of the SJ is meaningful, leading a vortex strength reduction, with respect to the baseline case, of about 38%, 55%, 65%, and 53% at $z/c = 0.1,\ 0.5,\ 1,\ 2$ respectively. By decreasing the SJ exit velocity, the jet vortex has been found to be very weak and it completely disappears by increasing the actuation frequency to $F^+ = 0.55$ as shown in Fig. 5e, 5f, 5g, and 5h for the wing model Ss04. As a result, the upward displacement of the vortex is reduced with respect to the previous controlled case. However, a huge impact on the streamwise vorticity peak is registered as well, with a maximum reduction of 50% at $z/c = 2$. Moreover, in both controlled cases the wingtip vortex appears to be more diffuse, hence covering a larger area around the mean vortex center moving downstream.

This behavior is confirmed in Fig. 6 where the geometrical characteristics of the vortex are reported for all the controlled cases tuned to

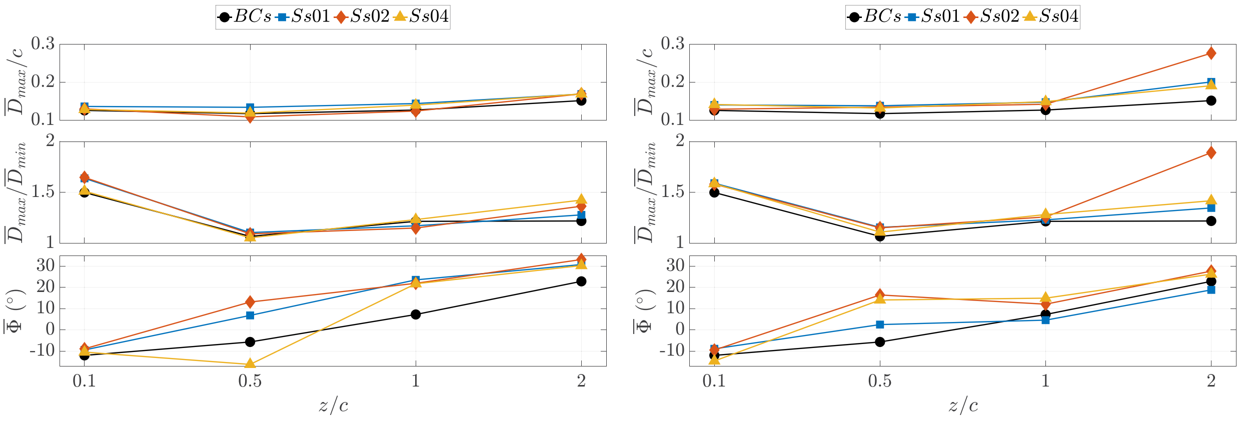

(a) $F^+ = 0.071$ (b) $F^+ = 0.55$

Fig. 6. Normalized time-averaged vortex major axis, aspect ratio and inclination angle for all the configurations investigated at $C_\mu = 0.2\%$.

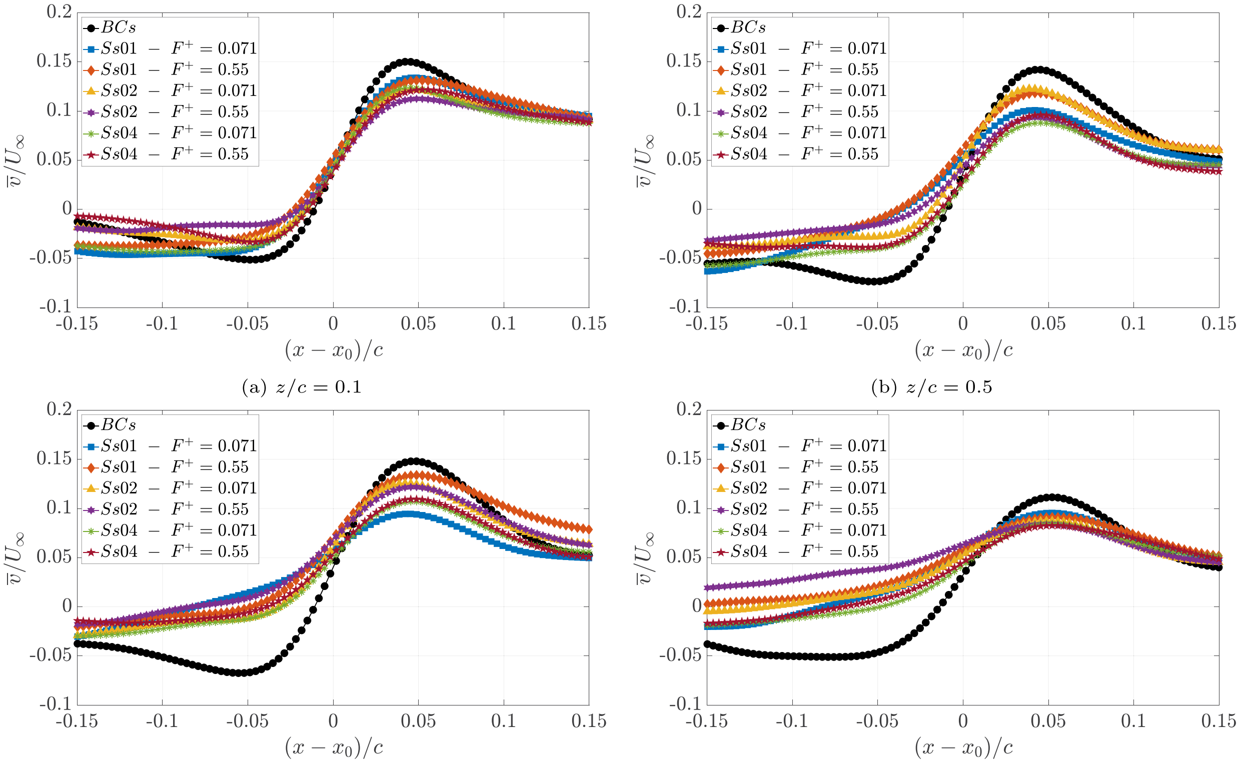

(a) $z/c = 0.1$ (b) $z/c = 0.5$

(c) $z/c = 1$ (d) $z/c = 2$

Fig. 7. Time-averaged radial distribution of the normalized circumferential velocity at different downstream positions for all the configuration investigated at $C_\mu = 0.2\%$.

the Crow ($F^+ = 0.071$) and Widnall ($F^+ = 0.55$) instability frequency. In particular, the most pronounced diffusion is related to the Ss02, $F^+ = 0.55$, where a major axis increase of about 82% with respect to the baseline case is observed at $z/c = 2$. As it can be noted in Fig. 6a, the vortex aspect ratio in each controlled case is maximized at $z/c = 0.1$ and it is slightly higher than the baseline case, meaning that the SJ actuation does not give rise to a significant stretching whilst causing a mean rotation of the vortex principal axis since the inclination angle $\overline{\Phi}$ increases with the actuation and downstream distance.

It is noted that the streamwise vorticity peak reduction obtained in the present work is comparable to the one achieved by Dghim et al. [48] at the downstream distance $z/c = 3$. With a momentum coefficient halved ($C_\mu = 0.1\%$) with respect to the controlled case of the present work, but with higher frequency ($F^+ = 0.96$), they obtained a decrease of the axial vorticity peak of 22% with respect to the baseline case against the reduction of at least 50% obtained for the present work at $z/c = 2$. Dghim et al. [48] demonstrated a similar streamwise vorticity peak reduction of 60% compared to the natural vortex case only with a higher $C_\mu = 1\%$ against the momentum coefficient of the present work equal to $C_\mu = 0.2\%$, suggesting that less power to generate the actuation would be sufficient to produce an equally effective control.

4.2. Circumferential velocity

The effect of the SJ actuation frequency on the wingtip vortices may be further quantified by evaluating the radial profiles of the mean circumferential velocity which is a crucial parameter for the induced rolling moment in a wake hazard. As a first step, Fig. 7 shows the distribution of the normalized time-averaged y velocity component $\overline{v}/U_\infty$ along the x-direction at $y = y_0$ (namely the y-coordinate corresponding to the vortex center position) for all the investigated control configurations. Such a distribution coincides with the radial profile of the circumferential velocity along the vortex diameter aligned to the wing span direction. It is important to note that in all the measurement planes, the circumferential velocity exhibits positive peaks with magnitudes that are at least 50% higher than that of the negative peaks. This behavior can be ascribed to the double induction caused by the tip vortex itself and by the neighboring one, both inducing an upward velocity. In the following, only the positive peaks are analyzed. The region between the ensemble-averaged vortex location and the radial location at which the peak value occurs is often referred to as the inner vortex region. For the case BCs at $z/c = 0.1$, a dimensionless circumferential velocity peak value of 0.15 is reached at a normalized radial location of about 0.043. Moving to $z/c = 2$, the peak is displaced to larger radial location ($r/c = 0.053$) reducing of 26%. This may be attributed to the increased roll-up of the shear layer with increased streamwise distance. With the actuation, the gradient of $\overline{v}/U_\infty$ at the vortex center is decreased of about 30% for each controlled case, which is the result of a more diffuse vortex. This is confirmed also by the degree of asymmetry which becomes more pronounced with the SJ blowing going downstream. This decrease in the core shear is accompanied by a remarkable decrease in the peak value of at least 10% for each controlled case and downstream distance, with a maximum drop of about 38% for the configuration of Ss04, $F^+ = 0.071$ at $z/c = 0.5$. In particular, the higher actuation frequency $F^+ = 0.55$ (i.e. Widnall instability frequency) generally outperforms the lower one in any test case with the only exception of the wing model Ss01 at $z/c = 0.5$ and 1 in which the tuned Crow instability leads to circumferential velocity 7% less intense.

Finally, blowing through a larger exit section (Ss04) leads to a striking reduction of $\overline{v}/U_\infty$ of 19%, 32%, 27%, and 26% (Ss04, $F^+ = 0.55$) at $z/c = 0.1$, 0.5, 1 and 2 respectively, which is a promising result. The effectiveness of the SJ actuation in promoting vortex diffusion is in agreement with both the works of Margaris and Gursul [45] and Dghmi et al. [49] and the previous work from the present authors [50].

Although crucial three-dimensional effects dominate the genesis of vortex roll-up and formation, Phillips [74] reported that the circumferential velocity profiles adopt a self-similar behavior in the wingtip vortex core, when $\overline{U}_\theta$ and r are normalized by the peak value, $\overline{U}_{\theta,m}$, and the corresponding radial location, r_c, respectively. The normalized radial positions are identified with the self-similar variable $\eta = r/r_c$. The profiles of the normalized circumferential velocities fit the following model equation:

$$\frac{\overline{U}_\theta}{\overline{U}_{\theta,m}} = \left(1 + \frac{1}{2\chi}\right)\frac{1}{\eta}\left(1 - e^{-\chi\eta^2}\right) \tag{7}$$

where χ is defined by $e^\chi = 1 + 2\chi$, yielding $\chi \approx 1.256$. The vortex model of Eq. (7) along with the experimental measurements are shown in Fig. 8. The circumferential velocity is here calculated as follows:

$$U_\theta(r,\theta) = \left(v - v_c\right)\cos\theta - \left(u - u_c\right)\sin\theta \tag{8}$$

where r and θ are the radial and azimuthal coordinates in the polar reference frame with origin in the vortex core center and u_c and v_c are the spanwise and transverse velocities of the vortex center, respectively. In particular, the values of U_θ at a given r are determined by averaging the values of the circumferential velocities along the whole circumference with radius equal to r sampled every 3.6 degrees.

Starting from the baseline configuration BCs, a good collapse with the theoretical fit inside the vortex core ($\eta \leq 1.2$) is clearly visible at $z/c = 0.1$. Also for larger downstream distances $z/c \geq 0.5$, the profiles of the normalized circumferential velocity collapse fairly well with the curve fit proposed by Phillips [74], indicating a self-similar vortex structure. It may be inferred that the roll-up process is almost completed at $z/c = 2$ and the vortex core has evolved asymptotically to reach a nearly axisymmetric distribution. However, a non-negligible variance of the radial profiles $\overline{U}_\theta/\overline{U}_{\theta,m}$ from the theoretical model can be detected outside the vortex core ($\eta \geq 1.2$). As suggested by Saffman [75], the lack of collapse can be caused by the gradual transition between the viscous core region and the outer region dominated by the irrotational flow of the rolling vortex sheet. Under the controlled cases tuned to the Crow instability frequency (Fig. 8b, 8c, 8d), the SJ actuation seems to not modify the structure of the vortex core as the $\overline{U}_\theta/\overline{U}_{\theta,m}$ continues to exhibit a reasonable collapse with the theoretical fit at all the downstream locations, suggesting an asymptotic state. Actually, in the outer region, a larger departure from the model with respect to the BCs case is registered. This behavior is representative of the SJ actuation effects on the region around the vortex core where high-turbulence mixing alleviates the velocity gradients and thus increases the outward diffusion of vorticity. On the other hand, under the controlled case tuned to the Widnall instability frequency (Fig. 8e, 8f, 8g), it is clear that the wingtip vortex does not exhibit a self-similar behavior. In fact, the vortex core structure is deeply modified when excited with a frequency equal to the Widnall instability one [54]. The slight upward departure from the theoretical model was observed in previous studies by Dghim et al. [48,49]. On the contrary, the actuation at higher F^+ appears to not follow the theoretical vortex model, as it can be noted in Fig. 8e, 8f, 8g. This unconventional trend may be ascribed to the smoothing of the velocity gradients and to the large turbulence levels around the vortex generated by the SJ blowing which may lead to a higher spreading rate along the radial direction, requiring larger downstream distances to achieve a self-similar state.

4.3. Circulation

Time-averaged vortex circulation represents a key parameter to evaluate the effect of the synthetic jet actuation on the wingtip vortices features and development. The results are displayed in Fig. 9. The vortex circulation is computed as the integral of the vorticity distribution given by the fitted model of Eq. (5) over the vortex region area.

As expected from the streamwise vorticity results, the SJ greatly affects the time-averaged vortex circulation causing a relevant reduction in each condition investigated of about 25% with respect to the baseline configuration BCs. The maximum SJ influence is registered for the wing configuration Ss01 at $z/c = 1$ for the Crow instability frequency ($F^+ = 0.071$) which leads to a striking reduction of the circulation of 52%. According to this metrics, higher SJ velocity can be more beneficial in the wingtip vortices alleviations. On the other hand, by increasing the actuation frequency ($F^+ = 0.55$), the intermediate wing model Ss02 has been found to be the best configuration which reduces the circulation more than 35% at each measurement plane. However, these results are in contrast with the previous findings [50] at $z/c = 3$, where an increase of the vortex circulation up to 29% has been demonstrated, which could be beneficial as well because the instability growth rate of the wingtip vortices is proportional to $\Gamma/2\pi b$ [54]. Margaris and Gursul [45] evaluated the circulation over a rectangle, defined as the area including all the vorticity above 5% of the streamwise vorticity peak value. They did not demonstrate a noticeable effect of the synthetic jet actuation on the total circulation which remains constant with the actuation frequency and at most 2% higher than the reference value, while Dghim et al. [48] evaluated only the radial distribution of the circulation at $z/c = 3$ finding a circulation decrease inside the vortex core due to the reduced vorticity, and an increase of around 10% outside the core region due to the vorticity diffusion over a larger area.

As already demonstrated for the circumferential velocity, the effect of the SJ actuation control on the wingtip vortex core structure can be examined from the radial distribution of the normalized circulation, $\overline{\Gamma}/\overline{\Gamma}_c$, plotted against the similarity variable, η, for different downstream positions in Fig. 10. Hoffmann and Joubert [76] suggested an empirical curve fitting relationship to analyze the circulation behavior

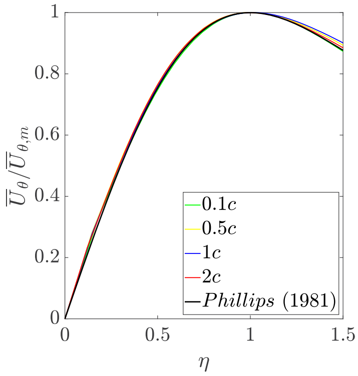

(a) BCs

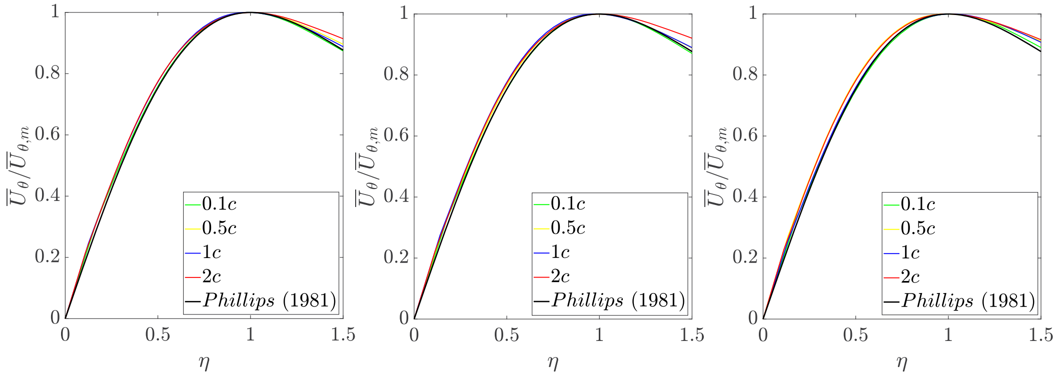

(b) $F^+ = 0.071$, Ss01 (c) $F^+ = 0.071$, Ss02 (d) $F^+ = 0.071$, Ss04

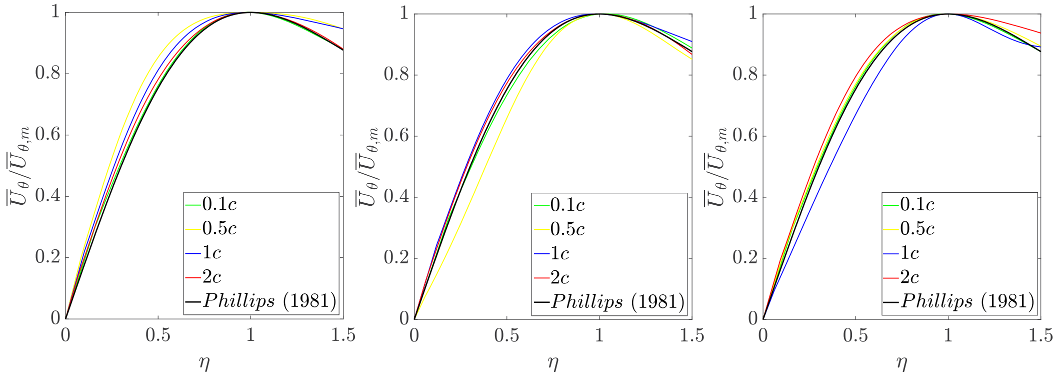

(e) $F^+ = 0.55$, Ss01 (f) $F^+ = 0.55$, Ss02 (g) $F^+ = 0.55$, Ss04

Fig. 8. Time-averaged radial profiles of the normalized circumferential velocity in a self-similar coordinates system at $C_\mu = 0.2\%$ and different downstream positions.

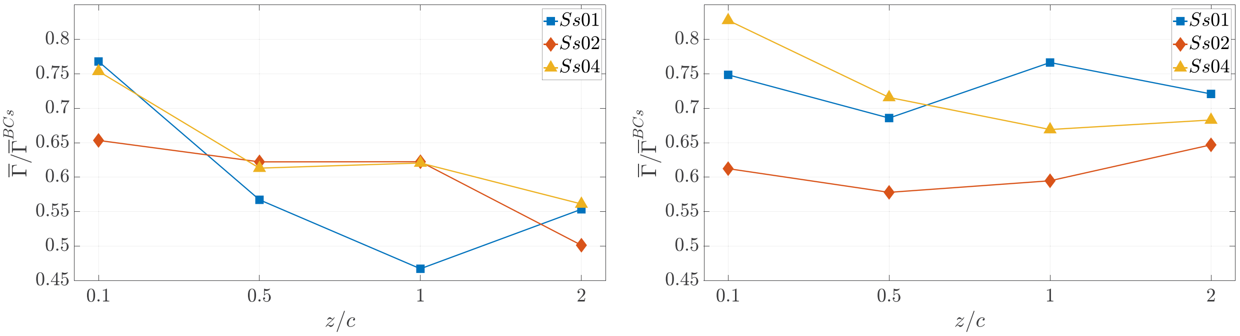

(a) $F^+ = 0.071$ (b) $F^+ = 0.55$

Fig. 9. Normalized time-averaged vortex circulation comparison with respect to the BCs for each configuration investigated at $C_\mu = 0.2\%$. The BCs values of $\overline{\Gamma}^{BCs}/cU_\infty$ are equal to 0.0443, 0.0424, 0.0433, 0.0404 at $z/c = 0.1,\ 0.5,\ 1,\ 2$ respectively.

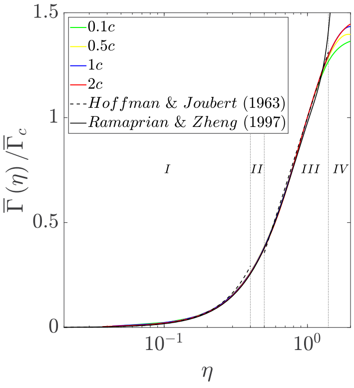

(a) BCs

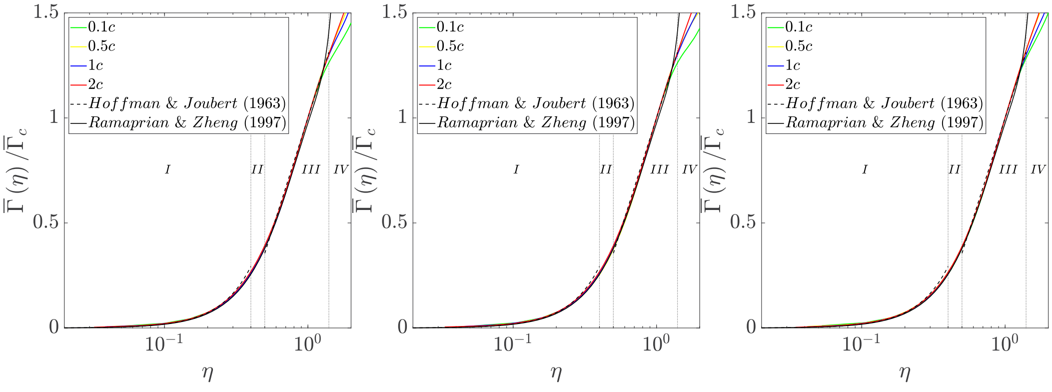

(b) $F^+ = 0.071$, Ss01 (c) $F^+ = 0.071$, Ss02 (d) $F^+ = 0.071$, Ss04

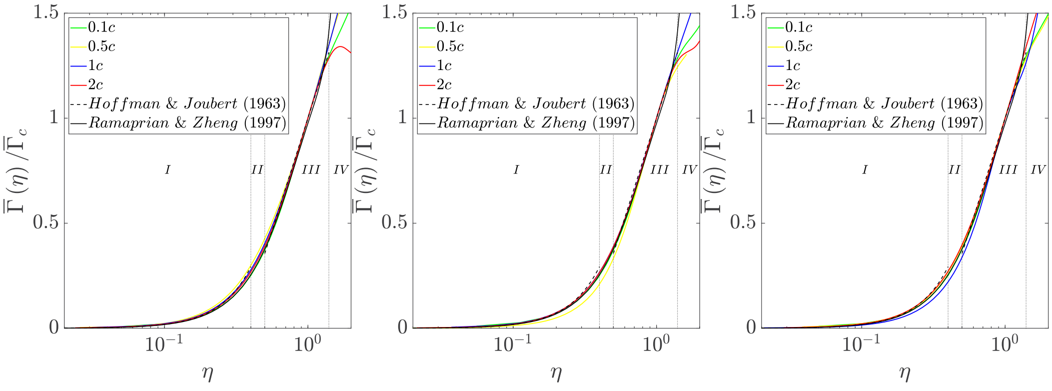

(e) $F^+ = 0.55$, Ss01 (f) $F^+ = 0.55$, Ss02 (g) $F^+ = 0.55$, Ss04

Fig. 10. Time-averaged self-similar circulation profiles of the inner region at $C_\mu = 0.2\%$ and different downstream positions: I, inner core; II, buffer region; III, logarithmic region; IV, outer region.

within the inner core and the logarithmic regions of the vortex according to the following expressions:

$$\frac{\overline{\Gamma}(\eta)}{\overline{\Gamma}_c} = A\eta^2 \quad \text{for } \eta < 0.4 \tag{9}$$

$$\frac{\overline{\Gamma}(\eta)}{\overline{\Gamma}_c} = 1 + B\log(\eta) \quad \text{for } 0.5 < \eta < 1.4 \tag{10}$$

where the constants A and B are 1.83 and 0.93, respectively. As it can be noted in Fig. 10a, the baseline configuration BCs shows a reasonable agreement with the curve fit equations (9) and (10). However, a departure is evident in the logarithmic and outer regions (III and IV), suggesting that the vortex has not reached a self-similar state yet and thus a perfectly complete roll-up. A better agreement has been noticed with the sixth-order polynomial suggested by Ramaprian and Zheng [77] and Birch et al. [78] following the expression

$$\frac{\overline{\Gamma}(\eta)}{\overline{\Gamma}_c} = a_0\eta^2 + a_1\eta^4 + a_2\eta^6 \tag{11}$$

where the constants a_0, a_1, and a_2 are 1.756, -1.044, and 0.263, respectively. The excellent agreement of both the baseline and controlled cases self-similar circulation profiles with the curve fit in the inner core region (I) indicates that this region is mainly dominated by the viscous effect where the vortex core has an approximately rigid-body rotation [76,79]. The lack of collapse in the outer region (IV) is present also for the controlled cases. In particular, when increasing the actuation frequency at $F^+ = 0.55$, the departure among the curves at the different measurement planes increases, meaning that the vortex core will re-

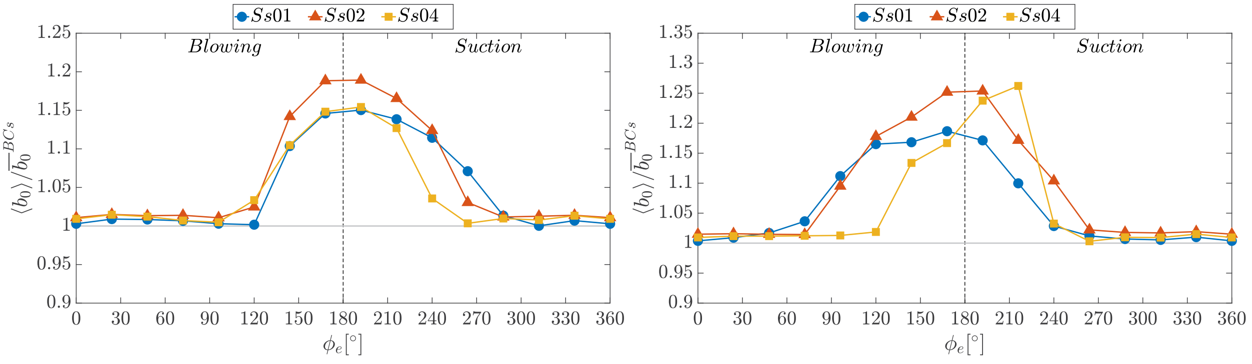

(a) $z/c = 0.1$ - $F^+ = 0.071$ (b) $z/c = 0.1$ - $F^+ = 0.55$

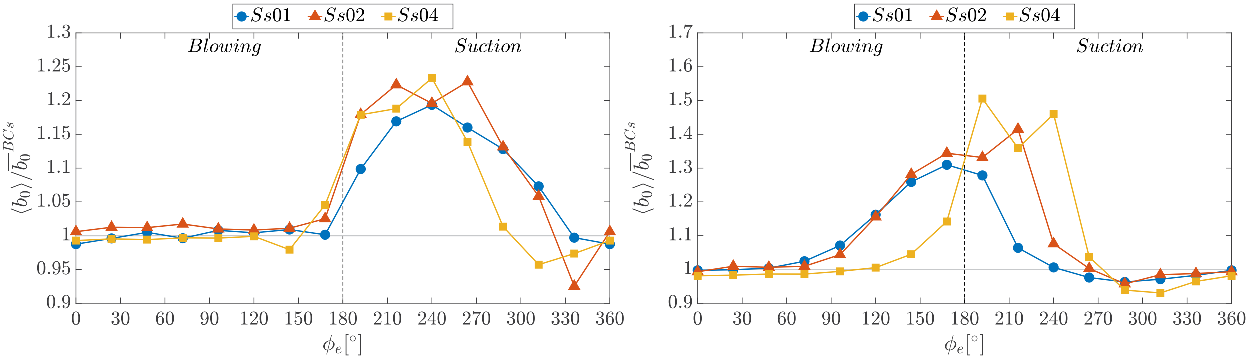

(c) $z/c = 2$ - $F^+ = 0.071$ (d) $z/c = 2$ - $F^+ = 0.55$

Fig. 11. Behavior of normalized phase-averaged vortices distance as a function of the phase of the electrical signal at different downstream positions for all the configurations investigated. The time-averaged BC values $\overline{b_0}^{BCs}/c$ are equal to 1.86 and 1.78 at $z/c = 0.1,\ 2$ respectively.

quire larger downstream distances to reach an asymptotic state due to outward diffusion caused by the SJ momentum injection.

5. Phase-averaged results

The phase-locked measurement results of the wingtip vortices are discussed in details in the present section. In all the following analyses, the phase $\phi = 0°$ is chosen as the phase at which the velocity field in the selected streamwise plane starts to feel the effect of the SJ ejection stroke. It is worth reminding that the velocimetry measurements are locked to the voltage input signal sent to the loudspeaker of the SJ actuator in the present experiments. The phase difference between the phase zero of the electrical signal ($\phi_e = 0°$) and the chosen phase zero ($\phi = 0°$) consists of two contributions: the phase difference between the electrical signal and the velocity response of the synthetic jet, which depends on the actuator geometry and the operating frequency, and the phase difference related to the convective propagation of the SJ disturbance from the jet slot exit to the measurement plane, which depends on the convective velocity U_c and the operating frequency according to $\Delta\phi_{conv} = 2\pi f \Delta z/U_c$ (being Δz the streamwise distance traveled by the disturbance). The first contribution can be easily determined by characterizing the frequency response of the SJ actuator, whereas the second contribution is more difficult to estimate since U_c is not known a priori. While U_c is expected to be the same order as U_∞, the choice $U_c = U_\infty$ might be inaccurate due to the momentum deficit in the vortex core. For such a reason, in the present study the determination of the phase $\phi = 0°$ is not based on the estimation of the two above-mentioned contributions; conversely, it relies on the velocimetry data related to the wingtip vortex phase evolution. In particular, for this purpose the phase evolution of the distance b_0 between the wing tip vortices forming at the opposite edges of the wing model is considered. Since the field of view is focused on only one tip vortex, b_0 is determined from the position of the vorticity peak by assuming that the vorticity distribution in the wake of the wing model is symmetric with respect to the wing middle plane. In such a way, being x_0 the spanwise location of the vortex center (see Section 3.2), the distance between the wingtip vortices is given by $b_0 = 2|x_0|$. The phase evolution of the ratio between the phase-averaged value of b_0 and the time-averaged value related to the baseline case $\overline{b_0}^{BCs}$ is reported in Fig. 11 for all the three wing models equipped with a SJ actuator, for the nearest and the farthest measurement planes and the two operating frequencies under examination. In these diagrams, the phase reported on the abscissa is the electrical phase ϕ_e. It is possible to notice that in each of the presented cases, there exists a phase in which $\langle b_0\rangle/\overline{b_0}^{BCs}$ starts to increase above unity before reaching a maximum and then decreasing again. This phase can be assumed as the one at which the velocity field starts to feel the effect of the SJ ejection stroke; in fact, the momentum flux associated with the jet issuing through the slot causes the wing tip vortex to move outward (and downward) after the merging with the SJ primary vortex as shown in the following. In the current study, such a phase is calculated via a discrete Fourirer analysis of the $\langle b_0\rangle$ curves reported in Fig. 11. Fig. 12 shows these same curves in the new phase space where for $\phi = 0°$ the ejection stroke starts to affect the flow field in the investigated plane. In conclusion, it is noticed that the method used here to estimate the initial phase has been validated for the measurements related to $z/c = 0.1$. In this case, $\Delta\phi_{conv}$ is few degrees since z is small and the chosen zero phase in fact coincides with the beginning of the blowing phase of the SJ cycle, which was determined via the characterization of the SJ actuator frequency response.

5.1. Streamwise vorticity and geometrical features

The phase-evolution of the normalized streamwise vorticity peak is reported in Fig. 13 for each control configuration investigated at different downstream positions.

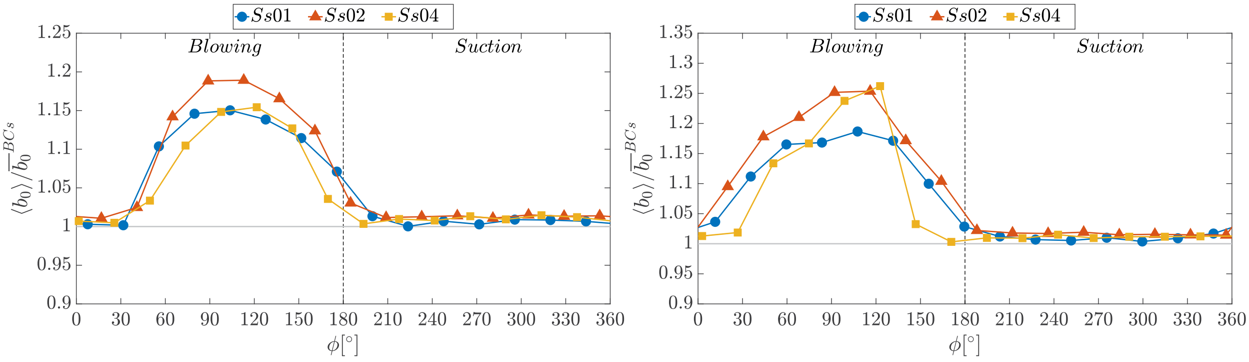

(a) $z/c = 0.1$ - $F^+ = 0.071$ (b) $z/c = 0.1$ - $F^+ = 0.55$

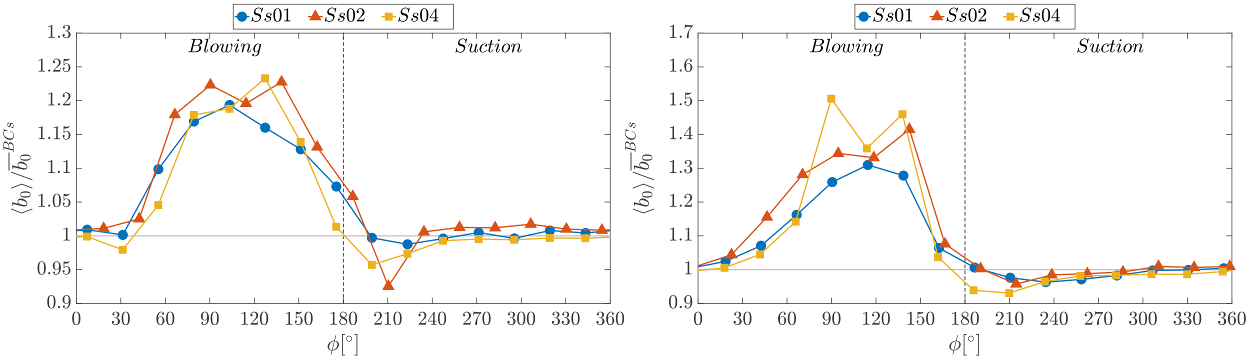

(c) $z/c = 2$ - $F^+ = 0.071$ (d) $z/c = 2$ - $F^+ = 0.55$

Fig. 12. Behavior of normalized phase-averaged vortices distance as a function of the phase ϕ (see the text for explanation) at different downstream positions for all the configurations investigated. The time-averaged BC values $\overline{b_0}^{BCs}/c$ are equal to 1.86 and 1.78 at $z/c = 0.1,\ 2$ respectively.

When the SJ is tuned to the Crow instability frequency at low $F^+ = 0.071$ (Fig. 13a, 13c, 13e, 13g), it is evident that the SJ is largely impactful during the blowing phase. In such a phase, for all the examined configurations and in all the investigated planes, the interaction of the SJ with the wing tip vortex results initially in a reduction of the vortex strength, which covers approximately the first quarter of the blowing phase. This is associated with a weakening of the rollup process caused by the SJ ejection. Such a behavior is followed by an increase up to a maximum value (reached between 90° and 135°), before a new drop which is completed at the beginning of the suction phase. The latter trend is associated with the evolution of the SJ primary vortex in the blowing phase, which intensifies with increasing values of the jet velocity and attenuates with decreasing values. In fact, as it is shown in the following, the SJ primary vortex and the wingtip vortex are co-rotating and merge in a single vortex downstream. Therefore, the SJ ejection has two competing effects on the wing tip vortex strength evolution: on one side, it produces a virtual increase of the wing span which favors a decrease of the vortex strength, on the other side, it results into a direct injection of vorticity into the wing tip vortex core which may cause its strengthening in proximity of the wing tip. This second effect is indeed dominating for the Ss01 case at $z/c = 0.1$ where the vortex strength is found to be greater than that of the natural vortex in the second half of the blowing phase. In all the remaining cases, however, the first above-mentioned effect is prevalent and a vorticity peak smaller than that of the baseline case is observed.

On the other side, during the suction phase the vortex strength keeps approximately constant and equal to or larger than the BC value especially for the two streamwise planes closest to the trailing edge ($z/c = 0.1$ and $z/c = 0.5$). As it will be shown later in this section, the wingtip vortices are pushed outward during the SJ blowing phase and they move back on the suction phase. As a result, the vortices interact more with the shear-layer leaving the trailing edge which could cause the vorticity enhancement.

However, it is possible to note that at each downstream location, increasing the SJ exit section area from the wing model Ss01 to a 4 times greater value of the wing model Ss04 leads to an even better performance in terms of streamwise vorticity peak reduction with respect to the baseline configuration, with reductions as large as 80% at $z/c = 2$. In particular, the wing model Ss04 with the greatest SJ exit section area (i.e. lower SJ exit velocity) outperforms the others with a streamwise vorticity peak reduction up of at least 60% during the SJ blowing phase at each downstream distance, which is promising.

It can be argued that blowing through a larger area allows the jets to interact more with the wingtip vortices resulting in a better performance of the synthetic jet active control. Actually, this behavior is confirmed in Fig. 13b, 13d, 13f, and 13h where the normalized streamwise vorticity peak of the SJ configurations tuned to the Widnall instability frequency ($F^+ = 0.55$) are reported. Here, a more sinusoidal phase-evolution is displayed, with again a greater efficiency during the SJ blowing phase where a maximum peak reduction around 80% is still attained for the wing model Ss04.

On the other side, during the SJ suction phase the streamwise vorticity peak nearly recovers the baseline value (slightly greater values up to 30% are found for the wing model Ss01 at $z/c = 1$). This confirms the time-averaged results for which the maximum SJ effectiveness on wingtip vortices control is achieved by blowing at high actuation frequency.

In order to have a better and visual understanding of the SJ actuation effectiveness, the phase-averaged contour maps of the normalized streamwise vorticity $\langle\zeta\rangle c/U_\infty$ in the $z/c = 0.1$ plane are reported in Fig. 14 and 15 for the controlled configurations with $F^+ = 0.071$ and $F^+ = 0.55$ for the models Ss01 and Ss04 respectively. The horizontal dashed black line represents the wing trailing edge projection on the measurement plane. Since from Fig. 13 it is possible to notice different phases in which the behavior of the streamwise vorticity peak is very

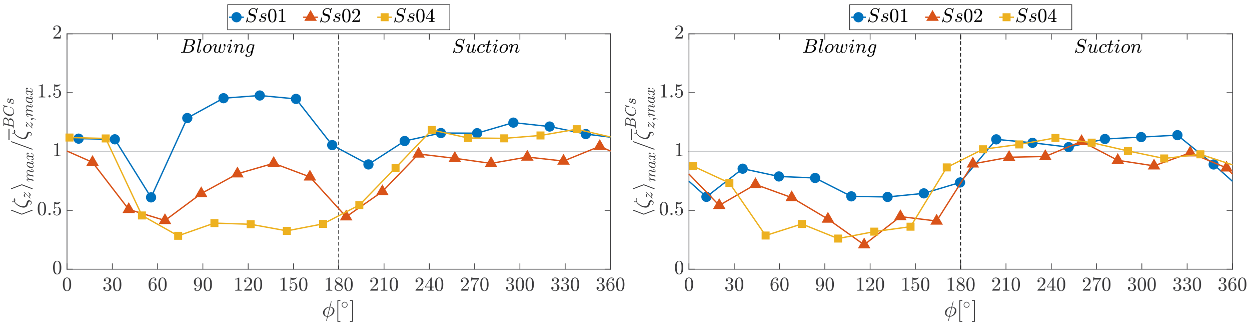

(a) $z/c = 0.1$ - $F^+ = 0.071$
(b) $z/c = 0.1$ - $F^+ = 0.55$

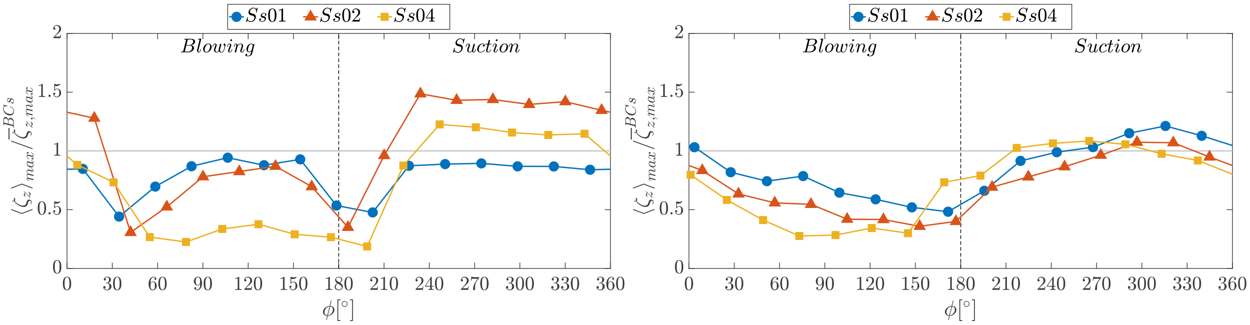

(c) $z/c = 0.5$ - $F^+ = 0.071$
(d) $z/c = 0.5$ - $F^+ = 0.55$

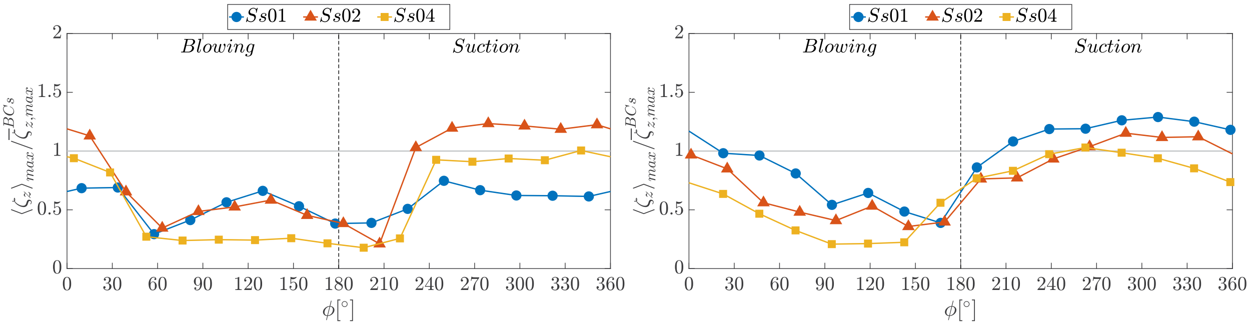

(e) $z/c = 1$ - $F^+ = 0.071$
(f) $z/c = 1$ - $F^+ = 0.55$

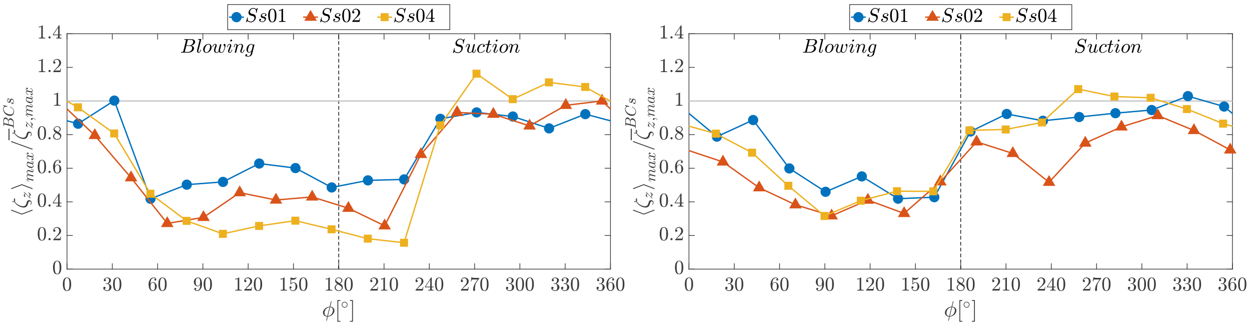

(g) $z/c = 2$ - $F^+ = 0.071$
(h) $z/c = 2$ - $F^+ = 0.55$

Fig. 13. Normalized phase-averaged streamwise vorticity peak at different downstream positions for all the configuration investigated. The time-averaged BCs values of $\overline{\zeta}^{BCs}_{z,max} c/U_\infty$ are equal to 10.5, 8.31, 8.26, 5.34 at $z/c = 0.1,\ 0.5,\ 1,\ 2$ respectively.

similar, for the sake of clarity, only half of the phase-averaged contour maps are presented.

At the lowest actuation frequency $F^+ = 0.071$ (Fig. 14), the tip vortex appears reinforced and overlapped to the jet vortex during the first part of the SJ blowing phase (a counter-rotating vortex is indeed visualized in the phases when the synthetic jet is issued) and moves back to a position very close to that of the BC configuration during the suction phase. The vortex shape is almost circular and in correspondence of the SJ maximum blowing it is diffused over an area larger than the uncontrolled case. During the suction phase, the SJ seems to be less effective since the baseline characteristics are restored.

Finally, from Figs. 14-15 it is possible to notice that a further effect of the synthetic jet control is represented by the movement of the vortex from the baseline position which is located in correspondence of the wing trailing edge projection and about $0.07c$ inward. The phase-evolution of the vortex centroids during the actuation is shown in Fig. 16(a, b), where the red cross indicates the time-averaged posi-

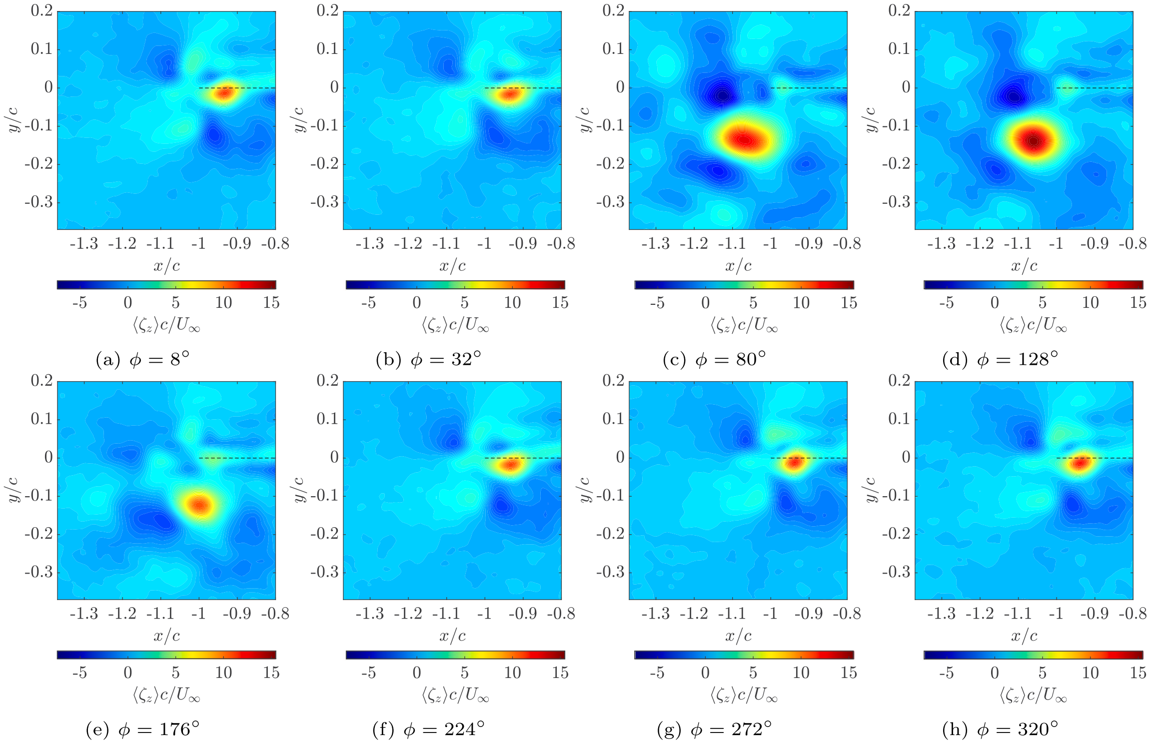

(a) $\phi = 8^\circ$ (b) $\phi = 32^\circ$ (c) $\phi = 80^\circ$ (d) $\phi = 128^\circ$

(e) $\phi = 176^\circ$ (f) $\phi = 224^\circ$ (g) $\phi = 272^\circ$ (h) $\phi = 320^\circ$

Fig. 14. Contour maps of the normalized phase-averaged streamwise vorticity fields at $z/c = 0.1$ for the wing model Ss01 at $F^+ = 0.071$.

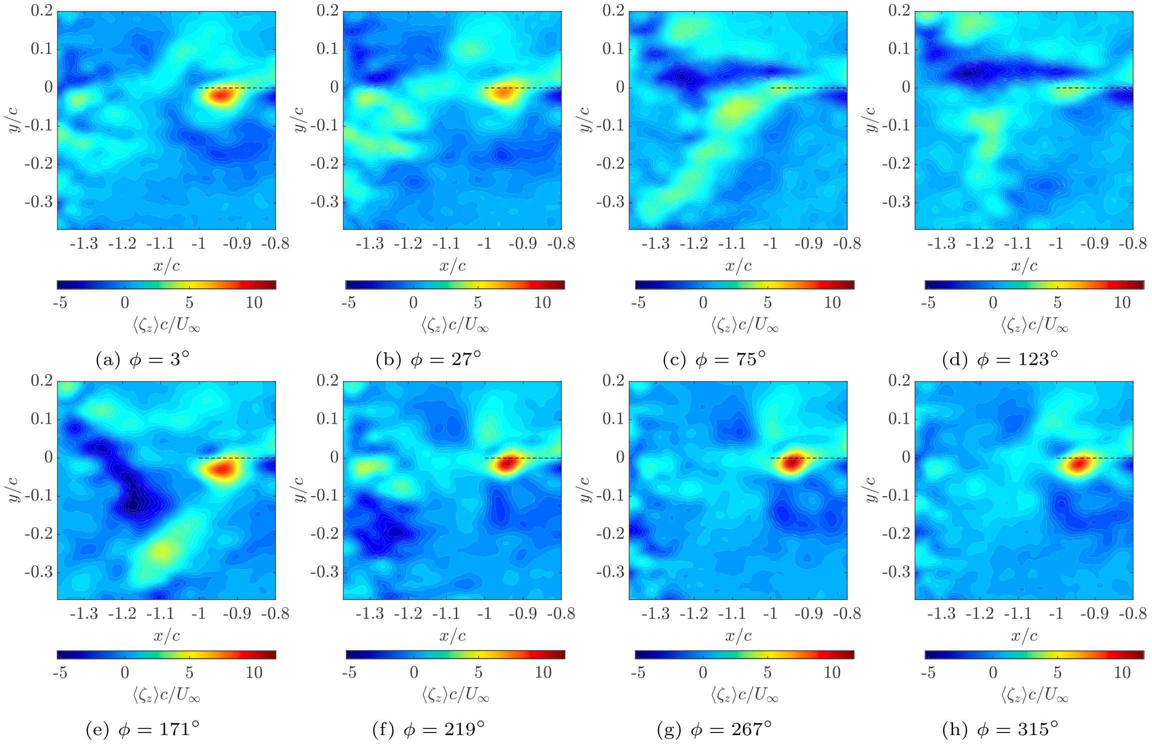

(a) $\phi = 3^\circ$ (b) $\phi = 27^\circ$ (c) $\phi = 75^\circ$ (d) $\phi = 123^\circ$

(e) $\phi = 171^\circ$ (f) $\phi = 219^\circ$ (g) $\phi = 267^\circ$ (h) $\phi = 315^\circ$

Fig. 15. Contour maps of the normalized phase-averaged streamwise vorticity fields at $z/c = 0.1$ for the wing model Ss04 at $F^+ = 0.55$.

tion of the wingtip vortex for the BC configuration. The black dashed line is again the projection of the trailing edge of the wing.

It is possible to notice in Fig. 16a that the synthetic jet actuation causes a periodic motion of the vortex at the Crow instability frequency configuration, moving the vortex about $0.14c$ both outboard and downward. In particular, the motion turns out to be limited to a direction inclined of 45° with respect to the wing span direction represented as a plain gray line, which could promote the Crow instability [54]. The same periodic behavior is obtained also for the configuration tuned at the Widnall instability frequency for the wing model Ss04 as reported in Fig. 16b.

At higher values of F^+, the vortex is pushed further outward, up to $0.24c$, and $0.1c$ downward, being the motion direction less inclined with respect to the previous case. This is clearly visible from the stream-

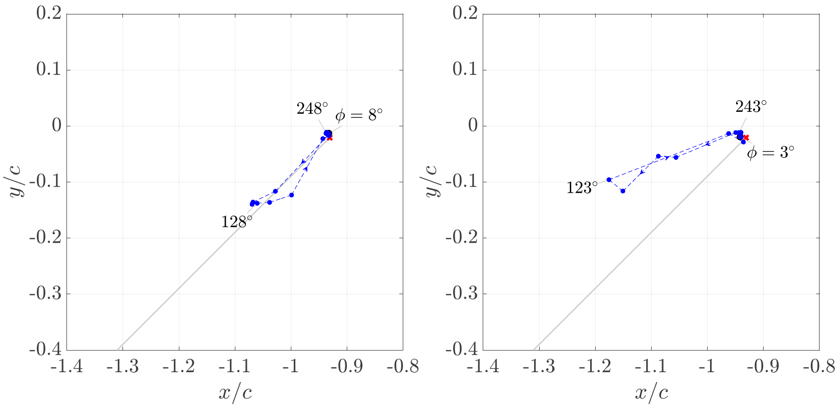

(a) $z/c = 0.1$ - $F^+ = 0.071$ - Ss01 (b) $z/c = 0.1$ - $F^+ = 0.55$ - Ss04

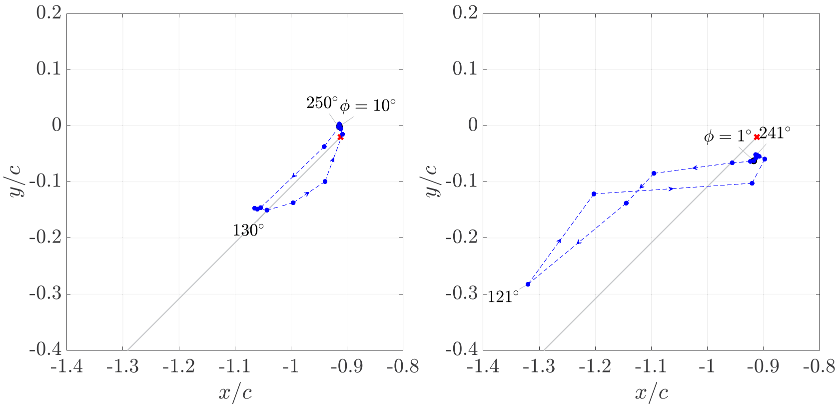

(c) $z/c = 0.5$ - $F^+ = 0.071$ - Ss01 (d) $z/c = 0.5$ - $F^+ = 0.55$ - Ss04.

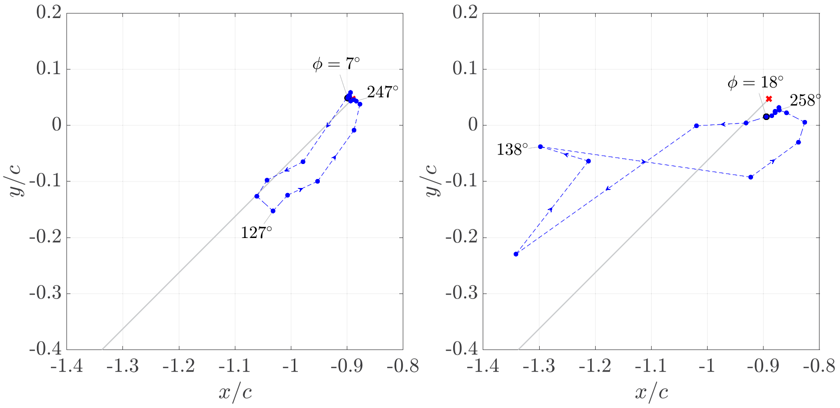

(e) $z/c = 2$ - $F^+ = 0.071$ - Ss01 (f) $z/c = 2$ - $F^+ = 0.55$ - Ss04

Fig. 16. Phase-averaged vortex center position at (a, b) $z/c = 0.1$, (c, d) $z/c = 0.5$ and (e, f) $z/c = 2$ for the wing model (a, c, e) Ss01 at $F^+ = 0.071$ and (b, d, f) Ss04 at $F^+ = 0.55$. The time-averaged BC position is marked with a red cross, while the gray line represents the 45° direction.

wise contour maps shown in Fig. 15. As already stated, the impact of the control configuration Ss04 at high actuation frequency is striking on the wingtip vortex strength reduction. In fact, during the SJ blowing phase, the vortex starts to lose its coherence being largely diffused with a very low value of the vorticity peak. The vortex diameter is four times larger than the baseline value and it is highly stretched, which could trigger large values of the shear rate, thus leading to a premature loss of coherence. However, the SJ is confirmed to be less effective during the suction phase also for the configuration at high actuation frequency, since the vortex recovers the vorticity distribution, the geometrical characteristics, and the position of the BC reference case.

At $z/c = 0.5$, the vorticity field contours reported in Fig. 17 for the wing model Ss01 at $F^+ = 0.071$ confirms the phase-evolution started at the previous location. From Fig. 17, it is possible to see clearly that the SJ ejection initially weakens the rollup process, thus reducing the wingtip strength (phase $\phi = 34°$). Subsequently, the wingtip vortex merges with the forming SJ primary vortex and at $\phi = 82°$ only one pair of counter-rotating vortices is indeed detectable. This vortex pair is displaced outward and downward with respect to the BC stationary wingtip vortex. In the following phases, while the SJ vortex loses its intensity, the wingtip vortex moves back to the BC position. As shown in Fig. 16(c, d), the maximum displacement is about $0.15c$ both along

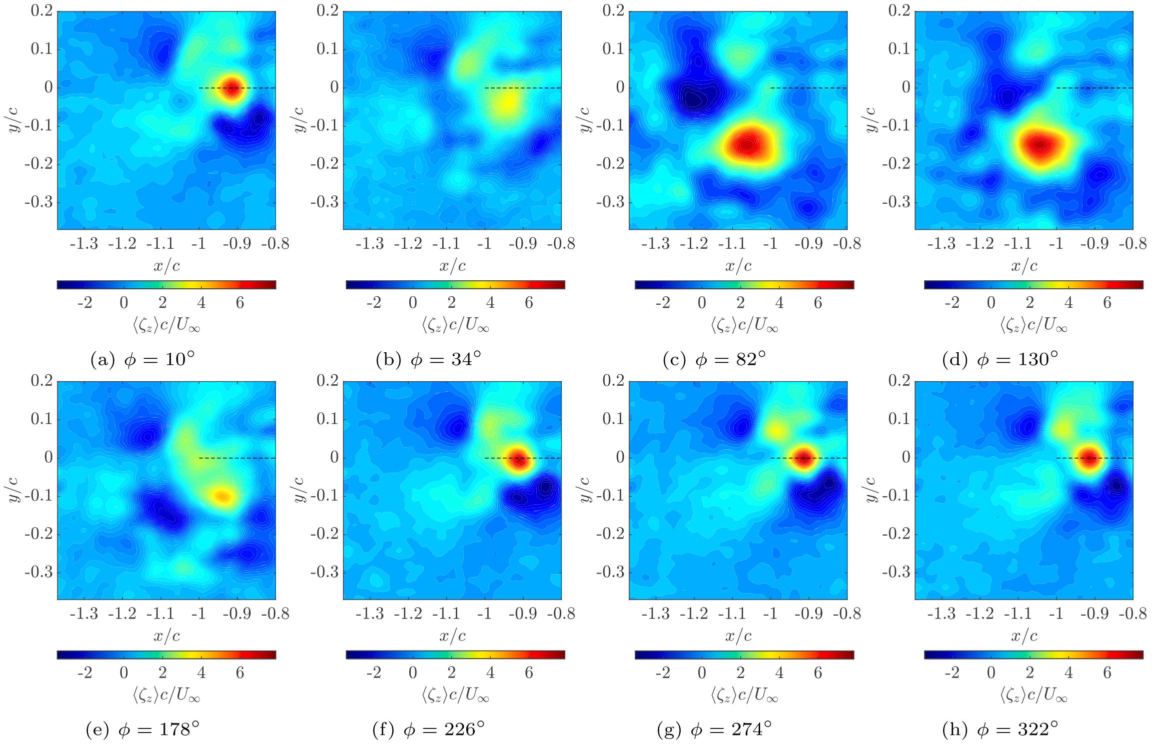

(a) $\phi = 10^\circ$ (b) $\phi = 34^\circ$ (c) $\phi = 82^\circ$ (d) $\phi = 130^\circ$

(e) $\phi = 178^\circ$ (f) $\phi = 226^\circ$ (g) $\phi = 274^\circ$ (h) $\phi = 322^\circ$

Fig. 17. Contour maps of the normalized phase-averaged streamwise vorticity fields at $z/c = 0.5$ for the wing model Ss01 at $F^+ = 0.071$.

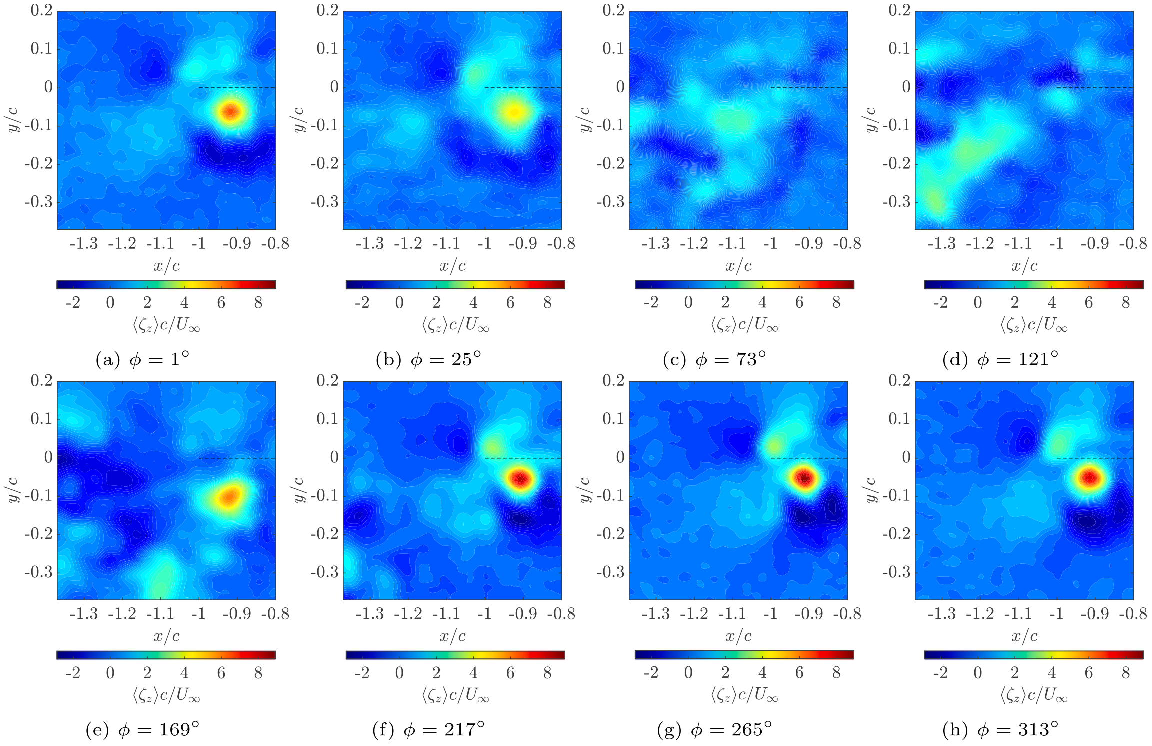

(a) $\phi = 1^\circ$ (b) $\phi = 25^\circ$ (c) $\phi = 73^\circ$ (d) $\phi = 121^\circ$

(e) $\phi = 169^\circ$ (f) $\phi = 217^\circ$ (g) $\phi = 265^\circ$ (h) $\phi = 313^\circ$

Fig. 18. Contour maps of the normalized phase-averaged streamwise vorticity fields at $z/c = 0.5$ for the wing model Ss04 at $F^+ = 0.55$.

the (negative) x and y directions and takes place essentially along the 45° direction, thus confirming the possibility of an early triggering of the Crow instability. However, the synthetic jet effectiveness is demonstrated only in the SJ blowing phase also in terms of the vortex position evolution (Fig. 16(c, d)) reaching a maximum displacement of about $0.15c$ both outboard and downward along a 45° direction, confirming the possibility of an early trigger of the Crow instability.

At a higher value of the actuation frequency, the synthetic jet penetrates more in the wingtip vortex leading to a very weak vorticity distribution in the middle part of the blowing period as shown in the contour maps reported in Fig. 18. The vortex continues losing its coherence due to the largely distributed turbulence injected through the high SJ exit section (Ss04) and it becomes barely detectable. Differently from the previous case, the configuration tuned to the Widnall instabil-

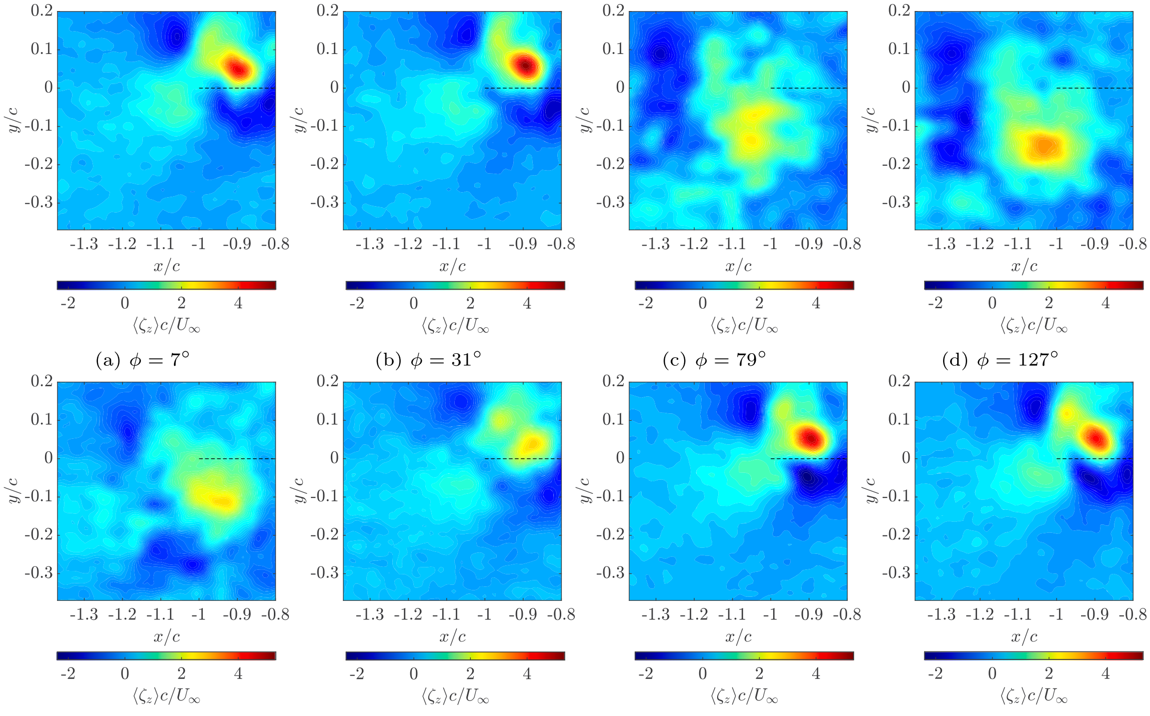

(a) $\phi = 7°$ (b) $\phi = 31°$ (c) $\phi = 79°$ (d) $\phi = 127°$

(e) $\phi = 175°$ (f) $\phi = 223°$ (g) $\phi = 271°$ (h) $\phi = 319°$

Fig. 19. Contour maps of the normalized phase-averaged streamwise vorticity fields at $z/c = 2$ for the wing model Ss01 at $F^+ = 0.071$.

ity causes a larger displacement of the vortex (see Fig. 16d) up to $0.4c$ outward and $0.22c$ downward still in a direction different from 45°. On the other hand, during the suction phase, the vorticity fields and the vortex features are very similar to the baseline configuration, confirming the loss of effectiveness of the synthetic jet.

For the sake of brevity, the phase-averaged vorticity results related to the downstream measurement plane at $z/c = 1$ are not reported, since the vortex features are very similar to the normalized vorticity contour maps at $z/c = 2$ shown in Fig. 19 and 20 for the wing model Ss01 and Ss04 at $F^+ = 0.071$ and $F^+ = 0.55$ respectively. Under the former control configuration, the wingtip vortex is noticeably weakened during the synthetic jet blowing phase and it is distributed over a wider area. During the suction phase, the vortex moves back to the baseline position which is located above the wing trailing edge projection due to the upwash induced by the couple of wingtip vortices generated by the negative lift of the wing. In particular, the baseline vorticity field is recovered also in this case and the presence of the jet vortex can be clearly detected from Figs. 19d-19g.

On the other hand, the synthetic jet configuration of the wing model Ss04 at higher $F^+ = 0.55$ is demonstrated to be strongly effective as shown in the normalized vorticity fields reported in Fig. 20. In the middle of the ejection phase, the wingtip vortex appears divided in different weak sub-vortices which then merge together during the suction phase where a clearly coherent structure is visible.

Lastly, in order to assess the variation of the vortex positions, a plot of the phase-evolution of the vortex centroids is reported in Fig. 16(e, f). Due to the upwash caused by the mutual induction of the couple of wingtip vortices generated by the finite wing, the majority of the phase-average positions are located above the wing trailing edge projection and they correspond to the synthetic jet suction phases. During the blowing phase, it is evident that the vortex is pushed downward and outward of about $0.2c$ and $0.55c$ for the configuration of Ss01 at $F^+ = 0.071$ and Ss04 at $F^+ = 0.55$ respectively. The periodic motion already found at the measurement planes close to the wing trailing edge is confirmed at $z/c = 2$. In particular, it can be noticed that moving downstream the vortex displacement increases especially when forcing at the Widnall instability frequency. On the other hand, moving the wingtip vortex outward can be beneficial for avoiding the blade-vortex-interaction noise in a rotor.

To summarize, according to the streamwise vorticity metric and the analysis of the geometrical characteristics of the wingtip vortex, the best control configuration is represented by the wing model with the largest synthetic jet exit section area (Ss04) at the higher actuation frequency tuned to the Widnall instability frequency ($F^+ = 0.55$). Moreover, the synthetic jet actuation has been demonstrated to reach the maximum effectiveness only during the blowing phase, while the baseline configuration features are restored during the suction phase. As such, the use of a pulsed jet could be a useful alternative to be investigated, but losing the advantage of a zero-net-mass-flux device, so the problem of harvesting the injected air remains open.

6. Conclusions

This paper focused on the experimental investigation of the effectiveness of synthetic jet actuation on the wingtip vortices and their wake hazard generated by an unswept, low aspect ratio, rectangular wing. The chosen model is justified by the need to preserve the mutual induction of the counter-rotating vortices during their evolution. Stereoscopic Particle Image Velocimetry was employed as measurement technique for the 2D-3C velocity measurements.

An experimental rig described in section 2 was designed based only on the actuation frequencies tuned to the Crow and Widnall instabilities. A fixed reference momentum coefficient of $C_\mu = 0.2\%$ was considered for the near-field investigation at the downstream distances from the wing trailing edge of $z/c = 0.1,\ 0.5,\ 1$ and 2. In addition to the baseline wing with a plain wing tip and no synthetic jet actuation, three squared-tipped wing models equipped with a $0.6c$-long SJ rectangular slot an increasing height of $0.01c$, $0.02c$, and $0.04c$ (namely Ss01, Ss02, and Ss04) were tested to analyze the effects of a variable SJ characteristic velocity U_0 at both actuation frequencies of $F^+ = 0.071$ and $F^+ = 0.55$ at fixed C_μ.

The results reported in section 4 confirm the striking effectiveness of the synthetic jet actuation in alleviating the wingtip vortices, since a time-averaged reduction of the streamwise vorticity of at least 25%

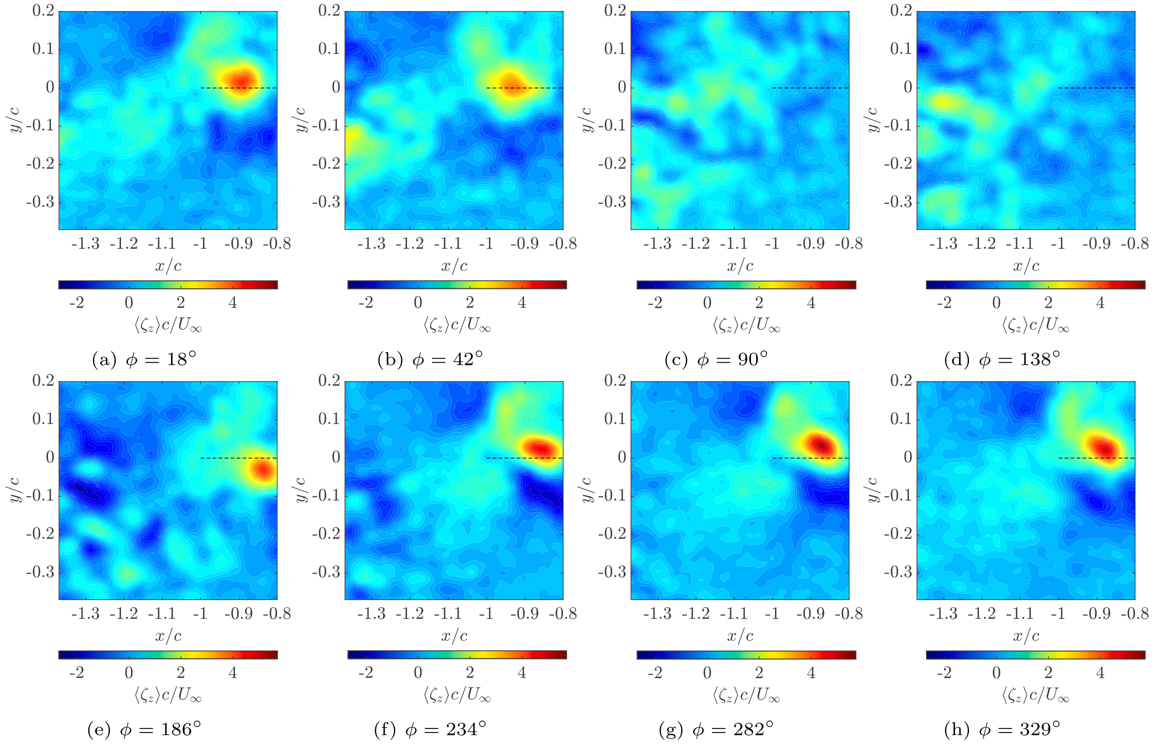

(a) $\phi = 18°$ (b) $\phi = 42°$ (c) $\phi = 90°$ (d) $\phi = 138°$

(e) $\phi = 186°$ (f) $\phi = 234°$ (g) $\phi = 282°$ (h) $\phi = 329°$

Fig. 20. Contour maps of the normalized phase-averaged streamwise vorticity fields at $z/c = 2$ for the wing model Ss04 at $F^+ = 0.55$.

is obtained at each downstream distance for each wing model tested at both actuation frequencies. However, a control strategy based on blowing through a large SJ exit section area leads to a more impactful wingtip vortices alleviation as confirmed by the phase-averaged results reported in section 5. The larger A_j, the larger the vorticity drop as shown i.e. for the $z/c = 2$ measurements at $F^+ = 0.071$ where a 40% and 80% of $\langle\zeta_z\rangle_{max}/\overline{\zeta}_{z,max}^{BCs}$ decrease is obtained for the Ss01 and Ss04 wing models respectively. Furthermore, the phase-evolution of the circumferential velocity peak confirms that the SJ configuration Ss04 (maximum A_j) has the best performance in reducing the wake-hazard since the value of $\langle U_\theta\rangle_{max}$ is reduced up to 50% which is noteworthy. The latter result is obtained at the frequency $F^+ = 0.55$ tuned to the Widnall instability, which represents the second ingredient for obtaining the most useful SJ device for the active control of the wingtip vortices in the near-field. In fact, increasing the actuation frequency, the Ss04 configuration allows to reach the minimum vorticity level, the maximum vortex diffusion with an increased diameter up to 3 times the baseline reference value, and low values of the vortex circulation. In addition, the periodic motion along a ±45° direction at which the vortex undergoes with the synthetic jet blowing is amplified at higher F^+, which can be beneficial for avoiding the blade-vortex-interaction noise in a rotor and for a premature instability development in the aircraft wake.

Declaration of competing interest

The authors declare the following financial interests/personal relationships which may be considered as potential competing interests: Carlo Salvatore Greco reports financial support was provided by Fondazione Compagnia di San Paolo.

Data availability

Data will be made available on request.

Acknowledgements

This research was supported by Università degli Studi di Napoli Federico II and Compagnia di San Paolo under the Finanziamento della Ricerca di Ateneo Program 2020. The authors wish to thank Mr. G. Sicardi and Ing. Marco Cannata for contributing to the realization of the experimental setup and Ing. Lorenzo Torrente for contributing to the experiments.

References

[1] P.R. Spalart, Airplane trailing vortices, Annu. Rev. Fluid Mech. 30 (1) (1998) 107–138, https://doi.org/10.1146/annurev.fluid.30.1.107.

[2] I. Kroo, Drag due to lift: concepts for prediction and reduction, Annu. Rev. Fluid Mech. 33 (1) (2001) 587–617, https://doi.org/10.1146/annurev.fluid.33.1.587.

[3] F.H. Schmitz, Rotor noise, in: Aeroacoustics of Flight Vehicles: Theory and Practice, Volume 1: Noise Sources, vol. 1, 1991, pp. 65–149.

[4] Y.H. Yu, Rotor blade-vortex interaction noise, Prog. Aerosp. Sci. 36 (2) (2000) 97–115, https://doi.org/10.1016/s0376-0421(99)00012-3.

[5] A. Brocklehurst, G. Barakos, A review of helicopter rotor blade tip shapes, Prog. Aerosp. Sci. 56 (2013) 35–74, https://doi.org/10.1016/j.paerosci.2012.06.003.

[6] J. Tangler, The design and testing of a tip to reduce blade slap, in: 31st Annual Forum of the American Helicopter Society, Washington, DC, 1975.

[7] D. Hoad, Helicopter model scale results of blade–vortex interaction impulsive noise as affected by tip modification, in: 36th Annual Forum of the American Helicopter Society, Washington, DC, 1980.

[8] M. Bhagwat, M. Franke, P. Martin, J. Leishman, Flow visualisation and measurement in the wake of a rotor with a subwing tip, in: 55th Annual Forum of the American Helicopter Society, Montreal, Canada, 1999.

[9] A. Brocklehurst, A. Pike, Reduction of bvi noise using a vane tip, in: AHS Specialists' Conference on Aerodynamics, Dynamics and Acoustics, San Francisco, 1994.

[10] K. McAlister, C. Tung, J. Heinech, Forced diffusion of trailing vorticity from a hovering rotor, in: 57th Annual Forum of the American Helicopter Society, Washington, DC, 2001.

[11] T. Ota, Y. Hashiguchi, T. Tsukahara, Bvi noise reduction research with canard blade tip, in: 27th European Rotorcraft Forum, Moscow, 2001, pp. 23.1–11.

[12] Z. Liu, L. Sankar, A. Hassan, Alteration of the tip vortex structure of a hovering rotor by blowing, in: 37th Aerospace Sciences Meeting and Exhibit, American Institute of Aeronautics and Astronautics, 1999.

[13] Z. Liu, L. Sankar, A. Hassan, Alteration of the tip vortex structure of a hovering rotor using oscillatory jet excitation, in: 38th Aerospace Sciences Meeting and Exhibit, American Institute of Aeronautics and Astronautics, 2000.

[14] Y.O. Han, J.G. Leishman, Investigation of helicopter rotor-blade-tip-vortex alleviation using a slotted tip, AIAA J. 42 (3) (2004) 524–535, https://doi.org/10.2514/1.3254.

[15] R. Vasilescu, S. Dancila, Rotor wake modifications in hover using unsteady spanwise blowing, in: 44th AIAA Aerospace Sciences Meeting and Exhibit, American Institute of Aeronautics and Astronautics, 2006.

[16] P. Gehlert, Z. Cherfane, G. Cafiero, J.C. Vassilicos, Effect of multiscale endplates on wing-tip vortex, AIAA J. 59 (5) (2021) 1614–1628, https://doi.org/10.2514/1.j059878.

[17] S.C.C. Bailey, S. Tavoularis, Measurements of the velocity field of a wing-tip vortex, wandering in grid turbulence, J. Fluid Mech. 601 (2008) 281–315, https://doi.org/10.1017/s0022112008000694.

[18] S.C. Crow, Stability theory for a pair of trailing vortices, AIAA J. 8 (12) (1970) 2172–2179, https://doi.org/10.2514/3.6083.

[19] S.E. Widnall, D. Bliss, A. Zalay, Theoretical and experimental study of the stability of a vortex pair, in: J.H. Olsen, A. Goldburg, M. Rogers (Eds.), Aircraft Wake Turbulence and Its Detection, Springer US, Boston, MA, 1971, pp. 305–338.

[20] S.E. Widnall, D.B. Bliss, C.Y. Tsai, The instability of short waves on a vortex ring, J. Fluid Mech. 66 (1) (1974) 35–47, https://doi.org/10.1017/s0022112074000048.

[21] D. Sipp, L. Jacquin, Widnall instabilities in vortex pairs, Phys. Fluids 15 (7) (2003) 1861–1874, https://doi.org/10.1063/1.1575752.

[22] V.J. Rossow, Theoretical study of lift-generated vortex wakes designed to avoid rollup, AIAA J. 13 (4) (1975) 476–484, https://doi.org/10.2514/3.49734.

[23] W.R. Graham, S.W. Park, T.B. Nickels, Trailing vortices from a wing with a notched lift distribution, AIAA J. 41 (9) (2003) 1835–1838, https://doi.org/10.2514/2.7305.

[24] V.R. Corsiglia, R.E. Dunham, Aircraft Wake-Vortex Minimization by Use of Flaps, NASA Ames Research Center, 1977.

[25] J.C. Patterson, Vortex attenuation obtained in the Langley vortex research facility, J. Aircr. 12 (9) (1975) 745–749, https://doi.org/10.2514/3.59865.

[26] L.W. Traub, S. Mani, S.F. Galls, O.K. Rediniotis, Application of the vortex breakdown phenomenon in the attenuation of trailing vortices, Aeronaut. J. 102 (1018) (1998) 439–444, https://doi.org/10.1017/S0001924000027676.

[27] D.R. Croom, Evaluation of flight spoilers for vortex alleviation, J. Aircr. 14 (8) (1977) 823–825, https://doi.org/10.2514/3.44620.

[28] V.J. Rossow, Effect of wing fins on lift-generated wakes, J. Aircr. 15 (3) (1978) 160–167, https://doi.org/10.2514/3.58335.

[29] I. Schell, E. Özger, D. Jacob, Influence of different flap settings on the wake-vortex structure of a rectangular wing with flaps and means of alleviation with wing fins, Aerosp. Sci. Technol. 4 (2) (2000) 79–90, https://doi.org/10.1016/s1270-9638(00)00120-6.

[30] E. Ozger, I. Schell, D. Jacob, On the structure and attenuation of an aircraft wake, J. Aircr. 38 (5) (2001) 878–887, https://doi.org/10.2514/2.2847.

[31] R. Schöll, C. Buxel, G. Neuwerth, Influence of spanwise loading and fins on extended near-field vortex wake, in: 44th AIAA Aerospace Sciences Meeting and Exhibit, American Institute of Aeronautics and Astronautics, 2006.

[32] H. Chevalier, Flight test studies of the formation and dissipation of trailing vortices, J. Aircr. 10 (1) (1973) 14–18, https://doi.org/10.2514/3.60193.

[33] S.C. Crow, E.R. Bate, Lifespan of trailing vortices in a turbulent atmosphere, J. Aircr. 13 (7) (1976) 476–482, https://doi.org/10.2514/3.44537.

[34] A. Bilanin, S. Widnall, Aircraft wake dissipation by sinusoidal instability and vortex breakdown, in: 11th Aerospace Sciences Meeting, American Institute of Aeronautics and Astronautics, 1973.

[35] M.R. Barber, J. Tymczyszyn, Wake vortex attenuation flight tests, Tech. Report, NASA CP-2170, Federal Aviation Administration, Los Angeles, CA, United States, Mar. 1980.

[36] F.L.J. Jordan, Flow visualization of the wake of a transport aircraft model withlateral-control oscillations, Tech. Report, NASA TM-84623, NASA Langley Research Center, Hampton, VA, United States, Jun. 1983.

[37] V.J. Rossow, Wake hazard alleviation associated with roll oscillations of wake-generating aircraft, J. Aircr. 23 (6) (1986) 484–491, https://doi.org/10.2514/3.45333.

[38] S. Haverkamp, G. Neuwerth, D. Jacob, Active and passive vortex wake mitigation using control surfaces, Aerosp. Sci. Technol. 9 (1) (2005) 5–18, https://doi.org/10.1016/j.ast.2004.08.005.

[39] C.G. Matalanis, J.K. Eaton, Wake vortex control using static segmented Gurney flaps, AIAA J. 45 (2) (2007) 321–328, https://doi.org/10.2514/1.25956.

[40] L.N. Cattafesta, M. Sheplak, Actuators for active flow control, Annu. Rev. Fluid Mech. 43 (1) (2011) 247–272, https://doi.org/10.1146/annurev-fluid-122109-160634.

[41] A.M. Edstrand, L.N. Cattafesta, Topology of a trailing vortex flow field with steady circulation control blowing, in: 53rd AIAA Aerospace Sciences Meeting, American Institute of Aeronautics and Astronautics, 2015.

[42] J.H. Garcìa-Ortiz, F.J. Blanco-Rodrìguez, L. Parras, C. del Pino, Experimental observations of the effects of spanwise blowing on the wingtip vortex evolution at low Reynolds numbers, Eur. J. Mech. B, Fluids 80 (2020) 133–145, https://doi.org/10.1016/j.euromechflu.2019.12.007.

[43] A.L. Heyes, D.A.R. Smith, Spatial perturbation of a wing-tip vortex using pulsed span-wise jets, Exp. Fluids 37 (1) (2004) 120–127, https://doi.org/10.1007/s00348-004-0791-5.

[44] B.L. Smith, A. Glezer, The formation and evolution of synthetic jets, Phys. Fluids 10 (9) (1998) 2281–2297, https://doi.org/10.1063/1.869828.

[45] P. Margaris, I. Gursul, Wing tip vortex control using synthetic jets, Aeronaut. J. 110 (1112) (2006) 673–681, https://doi.org/10.1017/s0001924000001536.

[46] P. Margaris, I. Gursul, Vortex topology of wing tip blowing, Aerosp. Sci. Technol. 14 (3) (2010) 143–160, https://doi.org/10.1016/j.ast.2009.11.008.

[47] M. Dghim, M. Ferchichi, R.E. Perez, M. BenChiekh, Near wake development of a wing tip vortex under the effect of synthetic jet actuation, Aerosp. Sci. Technol. 54 (2016) 88–107, https://doi.org/10.1016/j.ast.2016.04.008.

[48] M. Dghim, M. Ferchichi, H. Fellouah, Mid-wake wing tip vortex dynamics with active flow control, Exp. Therm. Fluid Sci. 98 (2018) 38–55, https://doi.org/10.1016/j.expthermflusci.2018.05.011.

[49] M. Dghim, M. Ferchichi, H. Fellouah, On the effect of active flow control on the meandering of a wing-tip vortex, J. Fluid Mech. 896 (2020), https://doi.org/10.1017/jfm.2020.343.

[50] M. Zaccara, G. Paolillo, C.S. Greco, T. Astarita, G. Cardone, Flow control of wingtip vortices through synthetic jets, Exp. Therm. Fluid Sci. 130 (2022) 110489, https://doi.org/10.1016/j.expthermflusci.2021.110489.

[51] M. Zaccara, P. Bragança, C. Cuvier, G. Paolillo, T. Astarita, J.-M. Foucaut, G. Cardone, C. Greco, Far field behaviour of wingtip vortices under synthetic-jet based control, Aerosp. Sci. Technol. 143 (2023) 108755, https://doi.org/10.1016/j.ast.2023.108755.

[52] D. Lasagna, R. Donelli, F. De Gregorio, G. Iuso, Effects of a trapped vortex cell on a thick wing airfoil, Exp. Fluids 51 (5) (2011) 1369–1384.

[53] C.S. Greco, A. Ianiro, T. Astarita, G. Cardone, On the near field of single and twin circular synthetic air jets, Int. J. Heat Fluid Flow 44 (2013) 41–52, https://doi.org/10.1016/j.ijheatfluidflow.2013.03.018.

[54] C. Breitsamter, Wake vortex characteristics of transport aircraft, Prog. Aerosp. Sci. 47 (2) (2011) 89–134, https://doi.org/10.1016/j.paerosci.2010.09.002.

[55] J.M. Ortega, R.L. Bristol, O. Savas, Experimental study of the instability of unequal-strength counter-rotating vortex pairs, J. Fluid Mech. 474 (2003) 35–84, https://doi.org/10.1017/s0022112002002446.

[56] T. Astarita, G. Cardone, Analysis of interpolation schemes for image deformation methods in PIV, Exp. Fluids 38 (2) (2004) 233–243, https://doi.org/10.1007/s00348-004-0902-3.

[57] T. Astarita, Analysis of interpolation schemes for image deformation methods in PIV: effect of noise on the accuracy and spatial resolution, Exp. Fluids 40 (6) (2006) 977–987, https://doi.org/10.1007/s00348-006-0139-4.

[58] T. Astarita, Analysis of weighting windows for image deformation methods in PIV, Exp. Fluids 43 (6) (2007) 859–872, https://doi.org/10.1007/s00348-007-0314-2.

[59] T. Astarita, Analysis of velocity interpolation schemes for image deformation methods in PIV, Exp. Fluids 45 (2) (2008) 257–266, https://doi.org/10.1007/s00348-008-0475-7.

[60] S.M. Mula, J.H. Stephenson, C.E. Tinney, J. Sirohi, Dynamical characteristics of the tip vortex from a four-bladed rotor in hover, Exp. Fluids 54 (10) (2013), https://doi.org/10.1007/s00348-013-1600-9.

[61] S.M. Mula, C.E. Tinney, A study of the turbulence within a spiralling vortex filament using proper orthogonal decomposition, J. Fluid Mech. 769 (2015) 570–589.

[62] I. Grant, Particle image velocimetry: a review, Proc. Inst. Mech. Eng., Part C, J. Mech. Eng. Sci. 211 (1) (1997) 55–76, https://doi.org/10.1243/0954406971521665.

[63] P. Martin, J. Leishman, G. Pugliese, S. Anderson, Stereoscopic piv measurements in the wake of a hovering rotor, in: American Helicopter Society 56th Annual Forum, Virginia, USA, 2000.

[64] S. Bhattacharya, J.J. Charonko, P.P. Vlachos, Stereo-particle image velocimetry uncertainty quantification, Meas. Sci. Technol. 28 (1) (2016) 015301, https://doi.org/10.1088/1361-6501/28/1/015301.

[65] A. Sciacchitano, B. Wieneke, PIV uncertainty propagation, Meas. Sci. Technol. 27 (8) (2016) 084006, https://doi.org/10.1088/0957-0233/27/8/084006.

[66] J. Zhou, R.J. Adrian, S. Balachandar, T.M. Kendall, Mechanisms for generating coherent packets of hairpin vortices in channel flow, J. Fluid Mech. 387 (1999) 353–396, https://doi.org/10.1017/s002211209900467x.

[67] J. Jeong, F. Hussain, On the identification of a vortex, J. Fluid Mech. 285 (1995) 69–94, https://doi.org/10.1017/s0022112095000462.

[68] R. Cucitore, M. Quadrio, A. Baron, On the effectiveness and limitations of local criteria for the identification of a vortex, Eur. J. Mech. B, Fluids 18 (2) (1999) 261–282, https://doi.org/10.1016/s0997-7546(99)80026-0.

[69] P. Chakraborty, S. Balachandar, R.J. Adrian, On the relationships between local vortex identification schemes, J. Fluid Mech. 535 (2005) 189–214, https://doi.org/10.1017/s0022112005004726.

[70] L. Graftieaux, M. Michard, N. Grosjean, Combining PIV, POD and vortex identification algorithms for the study of unsteady turbulent swirling flows, Meas. Sci. Technol. 12 (9) (2001) 1422–1429, https://doi.org/10.1088/0957-0233/12/9/307.

[71] G. Cafiero, G. Castrillo, C. Greco, T. Astarita, On the effects of square-fractal turbulators on the flow field generated by a synthetic jet actuator, Exp. Therm. Fluid Sci. 102 (2019) 302–315.

[72] F. De Gregorio, A. Visingardi, G. Iuso, An experimental-numerical investigation of the wake structure of a hovering rotor by piv combined with a $\gamma 2$ vortex detection criterion, Energies 14 (9) (2021) 2613.

[73] T. Leweke, S.L. Dizès, C.H. Williamson, Dynamics and instabilities of vortex pairs, Annu. Rev. Fluid Mech. 48 (1) (2016) 507–541, https://doi.org/10.1146/annurev-fluid-122414-034558.

[74] W.R.C. Phillips, The turbulent trailing vortex during roll-up, J. Fluid Mech. 105 (1) (1981) 451, https://doi.org/10.1017/s0022112081003285.

[75] P.G. Saffman, Vortex Dynamics, Cambridge University Press, 1993.

[76] E.R. Hoffmann, P.N. Joubert, Turbulent line vortices, J. Fluid Mech. 16 (03) (1963) 395, https://doi.org/10.1017/s0022112063000859.

[77] B.R. Ramaprian, Y. Zheng, Measurements in rollup region of the tip vortex from a rectangular wing, AIAA J. 35 (12) (1997) 1837–1843, https://doi.org/10.2514/2.59.

[78] D. Birch, T. Lee, F. Mokhtarian, F. Kafyeke, Structure and induced drag of a tip vortex, J. Aircr. 41 (5) (2004) 1138–1145, https://doi.org/10.2514/1.2707.

[79] W.J. Devenport, M.C. Rife, S.I. Liapis, G.J. Follin, The structure and development of a wing-tip vortex, J. Fluid Mech. 312 (1996) 67–106, https://doi.org/10.1017/s0022112096001929.